

# On the measurement of Sdiff splitting caused by lowermost mantle anisotropy

Jonathan Wolf<sup>1</sup>, Maureen D Long<sup>1</sup>, Neala Creasy<sup>2</sup>, and Edward Garnero<sup>3</sup>

<sup>1</sup>Yale University

<sup>2</sup>Los Alamos National Laboratory

<sup>3</sup>Arizona State University

December 7, 2022

## Abstract

Seismic anisotropy has been detected at many depths of the Earth, including its upper layers, the lowermost mantle, and the inner core. While upper mantle seismic anisotropy is relatively straightforward to resolve, lowermost mantle anisotropy has proven to be more complicated to measure. Due to their long, horizontal raypaths along the core-mantle boundary, S waves diffracted along the core-mantle boundary (Sdiff) are potentially strongly influenced by lowermost mantle anisotropy. Sdiff waves can be recorded over a large epicentral distance range and thus sample the lowermost mantle everywhere around the globe. Sdiff therefore represents a promising phase for studying lowermost mantle anisotropy; however, previous studies have pointed out some difficulties with the interpretation of differential SHdiff-SVdiff travel times in terms of seismic anisotropy. Here, we provide a new, comprehensive assessment of the usability of Sdiff waves to infer lowermost mantle anisotropy. Using both axisymmetric and fully 3D global wavefield simulations, we show that there are cases in which Sdiff can reliably detect and characterize deep mantle anisotropy when measuring traditional splitting parameters (as opposed to differential travel times). First, we analyze isotropic effects on Sdiff polarizations, including the influence of realistic velocity structure (such as 3D velocity heterogeneity and ultra-low velocity zones), the character of the lowermost mantle velocity gradient, mantle attenuation structure, and Earth's Coriolis force. Second, we evaluate effects of seismic anisotropy in both the upper and the lowermost mantle on SHdiff waves. In particular, we investigate how SHdiff waves are split by seismic anisotropy in the upper mantle near the source and how this anisotropic signature propagates to the receiver for a variety of lowermost mantle models. We demonstrate that, in particular and predictable cases, anisotropy leads to Sdiff splitting that can be clearly distinguished from other waveform effects. These results enable us to lay out a strategy for the analysis of Sdiff splitting due to anisotropy at the base of the mantle, which includes steps to help avoid potential pitfalls, with attention paid to the initial polarization of Sdiff and the influence of source-side anisotropy. We demonstrate our Sdiff splitting method using three earthquakes that occurred beneath the Celebes Sea, measured at many Transportable Array (TA) stations at a suitable epicentral distance. We resolve consistent and well-constrained Sdiff splitting parameters due to lowermost mantle anisotropy beneath the northeastern Pacific Ocean.

# On the measurement of $S_{\text{diff}}$ splitting caused by lowermost mantle anisotropy

Jonathan Wolf<sup>1,\*</sup>, Maureen D. Long<sup>1</sup>, Neala Creasy<sup>2,3</sup>, Edward Garnero<sup>4</sup>

---

## Abstract

Seismic anisotropy has been detected at many depths of the Earth, including its upper layers, the lowermost mantle, and the inner core. While upper mantle seismic anisotropy is relatively straightforward to resolve, lowermost mantle anisotropy has proven to be more complicated to measure. Due to their long, horizontal raypaths along the core-mantle boundary, S waves diffracted along the core-mantle boundary ( $S_{\text{diff}}$ ) are potentially strongly influenced by lowermost mantle anisotropy.  $S_{\text{diff}}$  waves can be recorded over a large epicentral distance range and thus sample the lowermost mantle everywhere around the globe.  $S_{\text{diff}}$  therefore represents a promising phase for studying lowermost mantle anisotropy; however, previous studies have pointed out some difficulties with the interpretation of differential  $SH_{\text{diff}}-SV_{\text{diff}}$  travel times in terms of seismic anisotropy. Here, we provide a new, comprehensive assessment of the usability of  $S_{\text{diff}}$  waves to infer lowermost mantle anisotropy. Using both axisymmetric and fully 3D global wavefield simulations, we show that there are cases in which  $S_{\text{diff}}$  can reliably detect and characterize deep mantle anisotropy when measuring traditional splitting parameters (as opposed to differential travel times). First, we analyze isotropic effects on  $S_{\text{diff}}$  polarizations, including the influence of realistic velocity structure (such as 3D velocity heterogeneity and ultra-low velocity zones), the character of the lowermost mantle velocity gradient, mantle attenuation structure, and Earth's Coriolis force. Second, we evaluate effects of seismic anisotropy in both the upper and the lowermost mantle on  $SH_{\text{diff}}$  waves. In particular, we investigate how  $SH_{\text{diff}}$  waves are split by seismic anisotropy in the upper mantle near the source and how this anisotropic signature propagates to the receiver for a variety of lowermost mantle models. We demonstrate that, in particular and predictable cases, anisotropy leads to  $S_{\text{diff}}$  splitting that can be clearly distinguished from other waveform effects. These results enable us to lay out a strategy for the analysis of  $S_{\text{diff}}$  splitting due to anisotropy at the base of the mantle, which includes steps to help avoid potential pitfalls, with attention paid to the initial polarization of  $S_{\text{diff}}$  and the influence of source-side anisotropy. We demonstrate our  $S_{\text{diff}}$  splitting method using three earthquakes that occurred beneath the Celebes Sea, measured at many Transportable Array (TA) stations at a suitable epicentral distance. We resolve consistent and well-constrained  $S_{\text{diff}}$  splitting parameters due to lowermost mantle anisotropy beneath

---

\*Corresponding author

*Email address:* [jonathan.wolf@yale.edu](mailto:jonathan.wolf@yale.edu) (Jonathan Wolf)

<sup>1</sup>Department of Earth and Planetary Sciences, Yale University, New Haven, CT, USA

<sup>2</sup>Los Alamos National Laboratory, Los Alamos, NM, USA

<sup>3</sup>Colorado School of Mines, Golden, CO, United States

<sup>4</sup>School of Earth and Space Exploration, Arizona State University, Tempe, AZ, USA

34 the northeastern Pacific Ocean.

Keywords: Planetary interiors, Numerical modelling, Computational seismology, Seismic anisotropy, Wave propagation

---

## 35 **1. Introduction**

36 Seismic anisotropy, or the directional dependence of seismic wave speeds, typically results  
37 from deformation in the Earth (e.g., Long and Becker, 2010). Seismic anisotropy has been  
38 identified in the crust (e.g., Barruol and Kern, 1996; Erdman et al., 2013), the upper mantle  
39 (e.g., Silver, 1996; Chang et al., 2014), the mantle transition zone (e.g., Yuan and Beghein,  
40 2014; Chang and Ferreira, 2019) and Earth’s inner core (e.g., Romanowicz et al., 2016;  
41 Frost et al., 2021). The bulk of the lower mantle is largely isotropic (e.g., Panning and  
42 Romanowicz, 2006), but some studies have suggested seismic anisotropy in the uppermost  
43 lower mantle, particularly in subduction zones (e.g., Foley and Long, 2011; Lynner and Long,  
44 2015; Mohiuddin et al., 2015; Ferreira et al., 2019). Finally, the bottom 200-300 km of the  
45 mantle, in the following synonymously referred to as  $D''$ , has been shown to be anisotropic  
46 in many places (e.g., Lay et al., 1998; Garnero et al., 2004; Wookey et al., 2005; Nowacki  
47 et al., 2010; Creasy et al., 2017; Wolf et al., 2019; Lutz et al., 2020; Wolf and Long, 2022).  
48 A main cause for seismic anisotropy is the preferential alignment of intrinsically anisotropic  
49 minerals due to mantle flow (e.g., Nowacki et al., 2011; Karato et al., 2008).

50 As with the upper mantle, measurements of lowermost mantle anisotropy can poten-  
51 tially resolve deep mantle deformation and map patterns of flow at the base of the mantle.  
52 In practice, however, such inferences remain challenging to make. These difficulties reflect  
53 shortcomings or assumptions in commonly used measurements methods (e.g., Nowacki and  
54 Wookey, 2016; Wolf et al., 2022a), limitations in data coverage (e.g., Ford et al., 2015;  
55 Creasy et al., 2017; Wolf et al., 2019), and/or uncertainties about realistic lowermost man-  
56 tle elasticity scenarios (e.g., Nowacki et al., 2011; Creasy et al., 2020). For instance, even  
57 with perfect knowledge about potential elastic tensors describing lowermost mantle mate-  
58 rials, seismic anisotropy must generally be measured from multiple directions to uniquely  
59 constrain deformation and mineralogy (e.g., Nowacki et al., 2011; Creasy et al., 2019). The  
60 deep mantle is likely dominantly composed of bridgmanite or its high-pressure polymorph  
61 post-perovskite, along with ferropericlase; the single-crystal elasticity and dominant slip  
62 systems of the minerals at the relevant pressure-temperature conditions are not precisely  
63 known (e.g., Creasy et al., 2020). Therefore, it is not completely straightforward to in-  
64 fer deformation geometry from measured shear wave splitting parameters (fast polarization  
65 directions and delay times). One strategy is to assume a plausible lowermost mantle com-  
66 position based on the likely temperature conditions and seismic velocities of a certain region

67 and carry out forward modelling to make predictions that can be compared to observations  
68 (e.g., Nowacki et al., 2010; Ford et al., 2015; Creasy et al., 2021; Wolf and Long, 2022).

69 Recent progress in full-wave modelling of seismic anisotropy with arbitrary geometries in  
70 the lowermost mantle has led to an improved understanding of the shortcomings inherent in  
71 commonly used shear wave splitting measurement techniques (Nowacki and Wookey, 2016;  
72 Tesoniero et al., 2020; Wolf et al., 2022a; 2022b), which are typically based on ray theory  
73 (a high-frequency approximation to the wave equation). However, not all of the difficulties  
74 have successfully been resolved, and challenges remain with commonly used measurement  
75 methods such as differential S-ScS and SKS-SKKS splitting. Thus, it is important to ex-  
76 plore alternatives to the commonly used seismic phases for measuring  $D''$  anisotropy, and  
77 to validate them using full-wave simulations rather than relying solely on ray-theoretical  
78 assumptions. A viable candidate phase for  $D''$  anisotropy measurements is the  $S_{\text{diff}}$  phase,  
79 because of its particularly long and horizontal raypaths along the CMB (Figure 1a), along  
80 which it can accumulate splitting. However, extracting information about deep mantle an-  
81 isotropy from  $S_{\text{diff}}$  waveforms is non-trivial. This is partly because  $S_{\text{diff}}$  waves are generally  
82 neither perfectly SH nor SV polarized in absence of anisotropy; furthermore,  $SH_{\text{diff}}$  and  
83  $SV_{\text{diff}}$  can accumulate a time shift due to isotropic structure (e.g., Komatitsch et al., 2010;  
84 Borgeaud et al.; 2016; Parisi et al., 2018), which can potentially be misinterpreted as shear  
85 wave splitting. Further, it must be ensured that phase interference is not misinterpreted  
86 as splitting (Komatitsch et al., 2010; Borgeaud et al.; 2016; Parisi et al., 2018). Another  
87 challenge is that the splitting signature of  $S_{\text{diff}}$  reflects the integrated effects of seismic an-  
88 isotropy along the raypath, including the source and receiver side upper mantle as well as  
89  $D''$ .

90 Despite these challenges, the interpretation of  $S_{\text{diff}}$  splitting in terms of lowermost mantle  
91 anisotropy has a substantial history (e.g., Vinnik et al., 1989; 1995; 1998a; 1998b; Garnero  
92 and Lay, 1997; Ritsema et al., 1998; Fouch et al., 2001). In some early papers,  $S_{\text{diff}}$  splitting  
93 was compared to the splitting of SK(K)S waves to assess the upper mantle anisotropy  
94 contribution to the waveforms, often under the assumption that  $SV_{\text{diff}}$  should have died  
95 off after travelling a certain epicentral distance, typically  $110^\circ$  (e.g., Vinnik et al., 1989).  
96 Alternatively, some studies have focused on the time delay between  $SH_{\text{diff}}$  and  $SV_{\text{diff}}$  without  
97 explicitly measuring splitting parameters (e.g., Ritsema et al., 1998; Fouch et al., 2001).  
98 While  $S_{\text{diff}}$  waves are in fact often primarily SH-polarized, recent work has shown that the  
99 assumption that  $SV_{\text{diff}}$  has completely died off at  $110^\circ$  distance cannot always be made  
100 (Komatitsch et al., 2010; Borgeaud et al., 2016). It has also been shown that the SH and  
101 SV components of S and  $S_{\text{diff}}$  (Komatitsch et al., 2010; Borgeaud et al., 2016; Parisi et al.,  
102 2018) can accumulate an apparent time-shift that can potentially mimic splitting, even

103 for isotropic Earth models. As a result, it has recently become less common to measure  
104  $D''$  seismic anisotropy using  $S_{\text{diff}}$ . A few exceptions (Cottaar and Romanowicz, 2013; Wolf  
105 and Long, 2022) have typically relied on specific arguments about likely initial polarizations  
106 of the waves under study.

107 In this study, we provide a new and comprehensive examination of the suitability of  $S_{\text{diff}}$   
108 splitting measurements to infer lowermost mantle anisotropy using global wavefield modeling  
109 tools. We analyze potential pitfalls in  $S_{\text{diff}}$  splitting analysis, and develop strategies to  
110 avoid them. For this purpose, we complement previous studies from Tesoniero et al. (2020)  
111 and Wolf et al. (2022a,b), who have analyzed the accuracy of commonly used shear-wave  
112 splitting techniques for  $D''$  anisotropy studies with a focus on SK(K)S and S/ScS. We also  
113 complement a recent study by Creasy et al. (in review), who investigated the effects of the  
114 Earth’s Coriolis force on SK(K)S polarizations. We undertake a similar approach as in these  
115 previous studies, using the AxiSEM3D (Leng et al., 2016, 2019) and SPECFEM3D\_GLOBE  
116 (Komatitsch and Tromp, 2002a, 2002b) software to model global wave propagation.

117 In contrast to previous studies (Komatitsch et al., 2010; Borgeaud et al., 2016; Parisi  
118 et al., 2018) that used global wavefield simulations to examine  $S_{\text{diff}}$  waveform behavior, we  
119 do not explicitly investigate differential  $SH_{\text{diff}}\text{-}SV_{\text{diff}}$  travel times. Rather, we analyze how  
120  $S_{\text{diff}}$  phases can be used infer robust shear-wave splitting parameters (time delay, fast-axis  
121 polarization direction, and splitting intensity) associated with lowermost mantle anisotropy.  
122 Unlike the measurement of differential  $SH_{\text{diff}}\text{-}SV_{\text{diff}}$  travel times, such an analysis includes  
123 strict requirements for the shape of the waveform. Whenever we use the term  $S_{\text{diff}}$ -splitting  
124 in the following, we refer to the explicit measurement of splitting parameters and not to the  
125 analysis of time delays.

126 We conduct a suite of global wavefield simulations with increasing complexity to assess  
127 the conditions under which  $S_{\text{diff}}$  waves are suitable for shear wave splitting measurements.  
128 In the first set of simulations, we analyse the effects of realistic isotropic velocity struc-  
129 ture on  $S_{\text{diff}}$  polarizations. In particular, we analyze the assumptions and conditions when  
130  $SV_{\text{diff}}$  and  $SH_{\text{diff}}$  die off. While it has been shown that assumptions cannot always be made  
131 (Komatitsch et al., 2010), no study so far has assessed these assumptions comprehensively.  
132 We continue with simulations investigating the effects of realistic 3D velocity structure and  
133 Earth’s Coriolis force on  $S_{\text{diff}}$  polarizations. In a second set of simulations, we investigate  
134 the effect of seismic anisotropy on  $SH_{\text{diff}}$  waves in detail. We examine the conditions un-  
135 der which splitting caused by source-side anisotropy could potentially be misdiagnosed as  
136 showing evidence for lowermost mantle anisotropy. Furthermore, we analyze the limits of  
137 resolution for the cases in which  $S_{\text{diff}}$  splitting can indeed be reliably attributed to lower-  
138 most mantle anisotropy. This second set of simulations reveals how exactly  $D''$  anisotropy

139 expresses itself in  $S_{\text{diff}}$  waveforms, particularly for cases in which there is also an upper  
140 mantle contribution. Finally, we use the insights gained for our  $S_{\text{diff}}$ -wavefield simulations  
141 to outline a novel strategy for using  $S_{\text{diff}}$  splitting measurements to reliably infer deep man-  
142 tle anisotropy. We use these insights to conduct a thorough splitting analysis for three  
143 deep earthquakes that occurred in the Celebes Sea in 2009 and 2010, for which  $S_{\text{diff}}$  waves,  
144 recorded at a large swath of stations across USArray, sample the lowermost mantle beneath  
145 the northeastern Pacific Ocean.

## 146 **2. Methods**

### 147 *2.1. Full-wave simulations*

148 AxiSEM3D and SPECFEM3D\_GLOBE are two commonly used tools to conduct global  
149 wavefield simulations. In this work, we primarily use AxiSEM3D due to its computational  
150 efficiency, which allows us to calculate synthetic seismograms down to periods that are  
151 commonly used for shear wave splitting measurements ( $\sim 5$ s). For these calculations, we  
152 extend the work of Tesoniero et al. (2020) and Wolf et al. (2022a,b), who have established  
153 AxiSEM3D as a suitable tool to conduct full-wave simulations for models that include  
154 anisotropy of arbitrary symmetry. To investigate the effects of Earth’s Coriolis force, we  
155 calculate seismograms down to  $\sim 9$ s using SPECFEM3D\_GLOBE, extending work from  
156 Creasy et al. (in review). The Coriolis force effect on body waves is frequency dependent,  
157 but because the period we are using in our SPECFEM3D\_GLOBE simulations (9 s) is much  
158 smaller than the period of Earth’s rotation, the results would be unaffected if we were to  
159 calculate synthetics for lower periods (Snieder et al., 2016). SPECFEM3D\_GLOBE gives  
160 the user the option to calculate synthetics with and without considering Earth’s rotation.

161 The initial input model for our numerical simulations with AxiSEM3D and SPECFEM3D\_GLOBE  
162 is isotropic PREM (Dziewonski and Anderson, 1981). All simulations include attenuation  
163 and ellipticity. Building on this simple scenario, we move towards increasingly complex  
164 models in our AxiSEM3D simulations. To do so, we replace the initial PREM input model  
165 at certain depths with different or more complex structure. Specifically, we first replace low-  
166 ermost mantle properties (e.g, velocity, velocity-gradient,  $Q_\mu$ ) in the context of an isotropic  
167 Earth to investigate the influence of various factors on how SH and SV amplitudes die off as  
168 a function of distance for diffracted waves. We also run simulations for a model that replaces  
169 PREM with 3D tomographic models to assess the influence of 3D velocity heterogeneity on  
170  $S_{\text{diff}}$  polarizations. Next, we shift our attention to simulations that include seismic aniso-  
171 tropy, in particular source-side and lowermost mantle anisotropy, for background models  
172 based on both PREM and PREM+3D tomographic model.

173 To identify the effects of Earth’s rotation on  $S_{\text{diff}}$  polarizations, we conduct simulations  
174 with SPECSEM3D\_GLOBE. In this solver, the globe is divided into six chunks; we apply 480  
175 spectral elements along one side of each chunk at the surface, resolving down to a minimum  
176 period of  $\sim 9$  s during simulations. We conduct two simulations including gravity (Cowling  
177 approximation) and the ocean load (Komatitsch and Tromp, 2002b), one including Earth’s  
178 rotation and the other excluding it. The source, at 616 km depth, is selected from the Global  
179 Centroid-Moment-Tensor catalogue (Ekström et al., 2012; event name: 201004112208A),  
180 but we change the source location to  $25^\circ\text{S}$  and  $66^\circ\text{W}$ . This event is selected so that the  
181 north-south propagation directions are far from the nodal planes of the source, to amplify  
182 the rotation effect (Creasy et al., in review). More than 1,000 pseudo receivers are placed  
183 across the global mesh with  $8^\circ$  - spacing. Waveforms from the simulations are bandpass  
184 filtered to retain energy between 10 – 50 s before processing.

185 An example of a typical source-receiver configuration used for our synthetic simulations  
186 with AxiSEM3D is shown in Figure 1b. Here, we place our source and receivers along the  
187 equator. The source is chosen to be at longitude  $-90^\circ$  and the receivers are placed along  
188 the equator at epicentral distances between  $103 - 130^\circ$ . For this scenario, we choose a focal  
189 depth of 500 km and a moment tensor whose only non-zero component is  $M_{tp}$  for perfect  
190 initial SH polarization. The same is done for perfect initial SV polarization (keeping  $M_{tt}$  as  
191 the only non-zero component). The details of the moment tensor are only relevant insofar  
192 as they affect the initial polarization of the wave; we choose these simple moment tensor  
193 scenarios because they are straightforward to understand and interpret. An additional  
194 source-receiver configuration that we use is an equivalent scenario along the zero meridian  
195 with the source at the north pole and a focal depth of 0 km. These two configurations  
196 are arbitrary, but they allow us to build on results from an initial benchmarking exercise  
197 without having to rerun computationally expensive simulations for another source-receiver  
198 setup. We use the first configuration (shown in Figure 1b) for all the isotropic AxiSEM3D  
199 simulations (Section 3) and the alternative configuration for all simulations that include  
200 lowermost mantle anisotropy (Section 4).

201 For simulations that include anisotropy near the source, we incorporate a 200 km thick  
202 layer with horizontally transversely isotropic (HTI) symmetry. We calculate appropriate  
203 elastic tensors using MSAT (Walker and Wookey, 2012), creating an elastic tensor at each  
204 depth increment whose isotropic average matches isotropic PREM velocities. We tune the  
205 elastic tensor using MSAT to have an anisotropic strength of either 2% or 4%. We incorpo-  
206 rate a source-side anisotropy layer at a depth range of 30 – 230 km for simulations with a  
207 source depth of 0 km, and at a depth range of 500 – 700 km for a focal depth of 500 km. In  
208 both cases the raypath through the layer is sufficiently vertical that the effects of focal depth

209 and anisotropic layer depth on the observed splitting are minor. Whenever we include upper  
 210 mantle anisotropy, we make sure that the HTI tensor is rotated such that its fast direction  
 211 is at an angle of  $45^\circ$  with respect to the polarization of the wave, which maximizes splitting.

212 For the lowermost mantle, we use an elastic tensor based on textured post-perovskite  
 213 (Ppv) from the elastic tensor library of Creasy et al. (2020), for simple shear with 100%  
 214 strain. This tensor incorporates estimates of single-crystal elasticity from Stackhouse et al.  
 215 (2005) and is based on a model of texture development using a visco-plastic self-consistent  
 216 modeling approach (Creasy et al., 2020). We rotate this tensor appropriately to obtain  
 217 strong  $S_{\text{diff}}$  splitting, following Wolf et al. (2022b). For the cases for which we measure  
 218 splitting intensities (Section 4), we mix this Ppv tensor with its isotropic equivalent (using  
 219 MSAT) to obtain an anisotropic strength that is only 1/3 of the original tensor. This allows  
 220 us to obtain more realistic splitting intensities ( $\sim 1$ ; Section 2.2) at the receiver when using  
 221 a global, uniform layer of anisotropy. In the real Earth, of course, some regions of  $D''$  may  
 222 be strongly anisotropic while others are isotropic. We emphasize that while we focus on a  
 223 Ppv anisotropy scenario in these simulations, our conclusions are more general and do not  
 224 depend on the details a certain elasticity scenario. Unless specified otherwise, the thickness  
 225 of the anisotropic basal mantle layer that we incorporate into our simulations is 150 km,  
 226 following previous work (Wolf et al., 2022a; 2022b).

## 227 2.2. Shear wave splitting measurements

228 A shear wave travelling through an anisotropic medium will split into two quasi-S wave  
 229 components, one fast and one slow (e.g., Silver and Chan, 1991). These quasi-S waves will  
 230 thus accumulate a time delay with respect to each other, usually referred to as  $\delta t$ . The fast  
 231 direction of the anisotropic material is inferred by measuring the fast polarization direction  
 232 of the wave, called  $\phi$ . The fast polarization direction,  $\phi$ , is usually measured as a (clockwise)  
 233 azimuth from the north. In this study, we also use  $\phi'$ , which denotes the fast polarization  
 234 direction measured clockwise from the backazimuthal direction (meaning that  $\phi$  is identical  
 235 to  $\phi'$  if the backazimuth is  $0^\circ$ ; Nowacki et al., 2010). Another quantity that is very useful for  
 236 studies of seismic anisotropy (in part due to its robustness in case of noise or weak splitting)  
 237 is the splitting intensity, in the following abbreviated as  $SI$  (Chevrot, 2000). The typical  
 238 definition of  $SI$  (for initially SV polarized waves) is

$$SI_{SV} = -2 \frac{T(t)R'(t)}{|R'(t)|^2} \approx \delta t \sin(2(\alpha - \phi)) , \quad (1)$$

239 with  $T(t)$  denoting the transverse component,  $R'(t)$  the time derivative of the radial com-  
 240 ponent,  $\delta t$  the time lag between the fast and slow travelling quasi S-waves, and  $\alpha$  the  
 241 polarization direction of the incoming wave (equivalent to the backazimuth for SKS waves

242 following their exit from the core). Thus,  $SI$  values are large if the transverse component  
 243 resembles the radial component time derivative (which is true in the case of splitting; Silver  
 244 and Chan, 1991; Chevrot, 2000) and has a high amplitude. The definition in Equation (1) is  
 245 usually used because splitting measurements are often made on \*KS phases that are initially  
 246 SV polarized due to the P-to-SV conversion at the CMB. For  $SH_{\text{diff}}$  waves, we will use an  
 247 alternate definition of  $SI$ :

$$SI_{SH} = -2 \frac{R(t)T'(t)}{|T'(t)|^2}, \quad (2)$$

248 where  $T'(t)$  denotes the transverse component time derivative. For these waves, when  $SH_{\text{diff}}$   
 249 undergoes splitting and some energy is partitioned into  $SV_{\text{diff}}$ , the transverse component  
 250 time derivative will have the shape of the radial component.

251 We bandpass-filter our synthetic and real data before measuring splitting, typically re-  
 252 taining periods between 8–25 s (for the assessment of Coriolis effects we instead use 10–25 s).  
 253 We conduct our splitting measurements on both synthetic and real data using a modified  
 254 version of the MATLAB-based graphical user interface SplitRacer (Reiss and Rumpker,  
 255 2017; Reiss et al., 2019). This version of SplitRacer retrieves the splitting parameters ( $\phi$ ,  
 256  $\delta t$ ) using the transverse energy minimization approach (Silver and Chan, 1991), paired with  
 257 the corrected error determination of Walsh et al. (2013); additionally, this version measures  
 258 the splitting intensity. We modified SplitRacer slightly for this study, measuring  $\phi'$  instead  
 259 of  $\phi$ , thus transforming  $\phi$  into the ray reference frame. We also switched the transverse  
 260 and radial components to estimate  $S_{\text{diff}}$  splitting. We call the fast polarization direction  
 261 obtained this way  $\phi''$ , which equals  $90^\circ - \phi'$ . This direction  $\phi''$  appears on many figures but  
 262 will also always be translated into the  $\phi'$  coordinate frame.

### 263 3. Isotropic effects on $S_{\text{diff}}$ waveforms

#### 264 3.1. Influence of various lowermost mantle properties on $S_{\text{diff}}$ amplitudes

265 First, we investigate the influence that different isotropic lowermost mantle properties  
 266 have on  $S_{\text{diff}}$  amplitudes, specifically on how  $S_{\text{diff}}$  amplitudes decrease as a function of dis-  
 267 tance in an isotropic Earth. Doornbos and Mondt (1979) and Komatitsch et al. (2010)  
 268 have previously shown how  $S_{\text{diff}}$  amplitudes decrease with distance, and that the relative  
 269 SV/SH amplitude ratio decrease depends on lowermost mantle properties. Here, we extend  
 270 this work and systematically examine the influence of a realistic range of lowermost mantle  
 271 properties on the amplitude decay with distance of  $SH_{\text{diff}}$  and  $SV_{\text{diff}}$ . Our motivation is to  
 272 identify whether it can be assumed, for different lowermost mantle structure and epicentral  
 273 distance ranges, that  $SV_{\text{diff}}$  has died off while  $SH_{\text{diff}}$  has not. This assumption is important

274 for S<sub>diff</sub> splitting analyses, as many studies presume that SH<sub>diff</sub> polarization energy domi-  
275 nates the S<sub>diff</sub> signal, due to the assumed die-off of SV<sub>diff</sub> polarization energy by a particular  
276 distance (e.g., Vinnik et al., 1989). While this assumption has been shown to be inadequate  
277 in some cases (Komatitsch et al., 2010; Borgeaud et al., 2016), it may be justified for some  
278 combinations of lowermost mantle conditions, which we interrogate here.

279 We show synthetic seismograms for the three scenarios shown in Figure 2. Scenario 1  
280 incorporates isotropic PREM and for scenarios 2 and 3, lowermost mantle velocities are  
281 decreased or increased, respectively. In the Supplementary Information, we additionally  
282 show some scenarios with different lowermost mantle velocity gradients (Figure S1) and a  
283 changed lowermost mantle shear wave attenuation (Figure S2).

284 The results for scenario 1 (isotropic PREM) are shown in Figure 3 for different initial  
285 polarizations of the S<sub>diff</sub> waves. We focus, in particular, on how radial and transverse am-  
286 plitudes decrease as a function of distance. We observe little or no interfering energy from  
287 other phases in the transverse component record sections for the entire distance range, al-  
288 though for SV there is some non-S<sub>diff</sub> energy for larger distances. While this SV energy does  
289 not correspond to any standard phase, we speculate that it comes from reflecting energy in  
290 the upper layers of the PREM input model, a phenomenon that has been observed before  
291 for ScS (Wolf et al., 2022b). Both SV and SH amplitudes are significant at distances of  
292 130°, although SV<sub>diff</sub> appears to die off slightly faster than SH<sub>diff</sub>. This simple simulation  
293 reinforces previous findings (Komatitsch et al., 2010; Borgeaud et al., 2016) that it is gener-  
294 ally incorrect to assume that for an S<sub>diff</sub> wave with arbitrary initial polarization, the initial  
295 SV<sub>diff</sub> energy has died off at a particular distance, while SH<sub>diff</sub> has not. We next extend  
296 on this scenario and examine how particular aspects of lowermost mantle structure affect  
297 SH<sub>diff</sub> and SV<sub>diff</sub> amplitudes.

298 We investigate the influence of reasonable velocity deviations (e.g., Simmons et al., 2010;  
299 French and Romanowicz, 2014) from PREM-like velocities, still in the context of 1D velocity  
300 profiles. We assume typical deviations of  $\sim \pm 2\%$  for LLVP regions and regions with higher  
301 velocities dominated by slab remnants, respectively. To have maximum radial and transverse  
302 amplitudes for visualization, we conduct two different end-member simulations, for initially  
303 solely SH and solely SV polarized S<sub>diff</sub> waves, respectively. The waveforms for simulations  
304 that incorporate such a change in lowermost mantle velocity are displayed in record sections  
305 in Figure 4, which uses similar plotting conventions as Figure 3. When velocities are higher  
306 than PREM, SH<sub>diff</sub> and SV<sub>diff</sub> amplitudes decrease similarly as a function of distance as  
307 for PREM. When velocities are lower than PREM, amplitudes decrease more slowly. While  
308 this is a general trend for both SH<sub>diff</sub> and SV<sub>diff</sub>, we find that SV<sub>diff</sub> energy dies off faster  
309 than SH<sub>diff</sub> for higher velocities, but behaves similarly as a function of distance for lower

310 velocities (Figure 4). This implies that the assumption that initial  $SV_{\text{diff}}$  energy has died off  
 311 at any particular distance, while  $SH_{\text{diff}}$  has not, will be more suitable (but still not perfect)  
 312 for faster than average regions in the lowermost mantle. The details of how  $SH_{\text{diff}}$ - and  
 313  $SV_{\text{diff}}$  die off, however, do not only depend on absolute lowermost mantle velocities but also  
 314 on the velocity gradient (Supplementary Figure S1). In Figure S1, we compare scenarios  
 315 that incorporate a velocity jump with linear velocity gradients at the base of the mantle.  
 316 For higher and lower velocities than average at the base of the mantle, a linear velocity  
 317 gradient will lead to a sharper amplitude decrease with distance than a velocity jump.

318 We next show that the mantle shear quality factor can have an influence on the amplitude  
 319 decrease of SH- and  $SV_{\text{diff}}$  waves.  $Q_{\mu}$  is usually assumed to have a value between 200 and  
 320 400 in radially symmetric models (e.g., Dziewonski and Anderson, 1981; Lawrence and  
 321 Wyession, 2006), although there may be a substantial lateral variability (e.g., Romanowicz  
 322 and Mitchell, 2007). To account for this, we test two relatively extreme cases with different  
 323  $Q_{\mu}$  values ( $Q_{\mu} = 75$  and  $Q_{\mu} = 1000$ ), leaving  $Q_{\kappa}$  unchanged. The results for both cases  
 324 are shown in Supplementary Figure S2. Changing  $Q_{\mu}$  appears to have a larger influence on  
 325  $SV_{\text{diff}}$  than  $SH_{\text{diff}}$ . While the details likely reflect the specific details of the implemented  
 326  $Q_{\mu}$  model, in general this implies that the propagation of initial  $SV_{\text{diff}}$  energy will not only  
 327 depend on the details of the lowermost mantle velocity and velocity gradient, but also on  
 328  $Q_{\mu}$ . This agrees with results from Borgeaud et al. (2016), who investigated the dependence  
 329 of apparent  $SH_{\text{diff}}$ - $SV_{\text{diff}}$  differential times on lowermost mantle  $Q_{\mu}$  structure in detail.

330 These simulations show that, although  $SV_{\text{diff}}$  dies off faster than  $SH_{\text{diff}}$  in most cases,  
 331 a blanket assumption that  $SV_{\text{diff}}$  dies off at a specific epicentral distance is unwarranted.  
 332 This is important because if SV energy is present for  $S_{\text{diff}}$  in absence of anisotropy, then  
 333 isotropic waveform effects can potentially be mistaken for splitting, even for isotropic Earth  
 334 models. For instance, Komatitsch et al. (2010), Borgeaud et al. (2016) and Parisi et al.  
 335 (2018) showed that isotropic structure can lead to a relative time-shift between  $SH_{\text{diff}}$  and  
 336  $SV_{\text{diff}}$  components (although the authors did not explicitly measure splitting). Our results  
 337 imply that  $S_{\text{diff}}$  waves can be used for shear wave splitting measurements only if it can  
 338 be established that, for a given event and raypath and in absence of lowermost mantle  
 339 anisotropy, the  $SV_{\text{diff}}$  component is expected to be negligible. This means that whether a  
 340 given measurement is usable will depend on the initial polarization of the wave as well as the  
 341 lowermost mantle structure. This criterion can be evaluated through synthetic modelling.  
 342 In practice, many  $S_{\text{diff}}$  waves will in fact be suitable for splitting analysis. Therefore, direct  
 343 S and ScS become asymptotic as they eventually become the same wave at the diffraction  
 344 distance. Their SV polarities, however, are opposite, resulting in destructive interference;  
 345 depending on the velocity structure, this can result in a rapidly diminishing  $SV_{\text{diff}}$  amplitude

346 with distance.

### 347 3.2. Influence of realistic 3D velocity structure on the polarizations of $S_{\text{diff}}$ waves

348 We have shown that  $S_{\text{diff}}$  waves with a significant initial SV component (that is, SV  
349 energy that does not result from splitting) cannot be reliably used for shear wave splitting  
350 measurements (Section 3.1). Therefore, from here on we will focus our attention on purely  
351 SH-polarized  $S_{\text{diff}}$  waves. In particular, we next investigate whether initially SH polarized  
352 waves can be influenced by effects other than anisotropy, such that some energy is partitioned  
353 into SV on the radial component, potentially mimicking splitting. We first investigate  
354 the effects of realistic 3D heterogeneity on  $S_{\text{diff}}$  polarizations. We do so by using the 3D  
355 tomography model GyPSuM (Simmons et al., 2010) in the mantle instead of our initial  
356 isotropic PREM input model; we retain PREM structure for the crust and the core. We  
357 place a source with a focal depth of 0 km at the north pole and the receivers every  $20^\circ$  along  
358 a specific longitude. We repeat this every  $20^\circ$  of longitude, starting at the zero meridian, for  
359 distances  $103 - 130^\circ$ . These waveforms are shown in Figure 5a for a representative example  
360 along longitude  $60^\circ$ . We see that almost no energy arrives on the radial component and  
361 the measured splitting intensities are null or very close to it ( $|SI| < 0.3$ ), consistent with  
362 a lack of splitting, for all measurements (Figure 5c). Receivers at other longitudes yield  
363 similar results. These simulations confirm that we cannot expect a significant redistribution  
364 of energy from the transverse to radial components (potentially mimicking splitting) when  
365 incorporating a realistic representative 3D tomographic model into our simulations. We  
366 repeat this exercise using the 3D tomography model S40RTS (Ritsema et al., 2011), which  
367 yields similar results in terms of shear wave polarizations (Figure S3).

368 We additionally conduct slightly more complicated simulations using the same GyPSuM-  
369 based input model and also including a global 20 km thick basal mantle layer of reduced  
370 shear velocities, approximating a global ultra-low velocity zone (ULVZ). ULVZs are thin  
371 features at the base of the mantle that are characterized by shear wave velocities that  
372 are reduced by some tens of per cent compared to the surrounding mantle (e.g., Yu and  
373 Garnero, 2018). A global ULVZ has not been observed; this simplified scenario may, however,  
374 be a good approximation for zones with widespread ULVZs. We implement S velocity  
375 reductions of 30% compared to PREM (decreasing P velocities by 10% and keeping density  
376 constant) and conduct simulations for an initially SH polarized  $S_{\text{diff}}$  wave with stations  
377 placed along the zero meridian. Waveforms are shown in Figure 5b as a function of distance  
378 and the corresponding splitting intensities are displayed in Figure 5d. We find that  $SI$ -  
379 values (representing the amount of radial component energy) are null ( $|SI| < |0.3|$ ) for all  
380 distances.

381 We conclude that, while  $SH_{\text{diff}}$  and  $SV_{\text{diff}}$  waves may indeed accumulate a relative time

382 shift in isotropic structure (Komatitsch et al., 2010; Borgeaud et al., 2016; Parisi et al., 2018),  
383 no substantial redistribution of energy from initially SH-polarized  $S_{\text{diff}}$  waves to  $SV_{\text{diff}}$  can be  
384 expected in realistic 3D tomographic models or through the influence of ULVZs. In cases for  
385 which a slight energy redistribution happens, the waveforms will be strongly distorted from  
386 the pulse shape predicted for shear wave splitting and, in practice, would not be mistaken  
387 for true splitting.

### 388 *3.3. Polarization anomalies caused by Earth’s Coriolis effect*

389 We next evaluate the influence of Earth’s Coriolis effect on  $S_{\text{diff}}$  waveforms using SPEC-FEM3D-GLOBE.  
390 The Earth’s Coriolis effect influences all seismic wave propagation, but it has the most no-  
391 ticeable effect on normal modes (Backus and Gilbert, 1961; Masters et al., 1983; Dahlen and  
392 Tromp, 1998) and surface waves (e.g., Park and Gilbert, 1986; Tromp, 1994; Snieder and  
393 Sens-Schönfelder, 2021). Body waves, particularly shear waves, can be modestly affected  
394 (Schoenberg and Censor, 1973; Snieder et al., 2016). As a shear wave propagates through  
395 a rotating body, there is a slow rotation of the polarization of shear waves; in contrast, the  
396 orientation of wavefronts is not affected by Earth’s rotation. The exact change in the polar-  
397 ization of a shear wave will depend on travel time duration, event location, and the raypath  
398 relative to Earth’s rotation axis, as outlined by Snieder et al. (2016). Here, we determine  
399 the deviations of  $S_{\text{diff}}$  from its initial polarization due to the Coriolis effect by comparing  
400 two simulations with the same event-receiver setup, for which one simulation excludes and  
401 the other includes Earth’s rotation (Figure 6).

402 We find that  $S_{\text{diff}}$  polarization anomalies follow the expected pattern of polarization  
403 change due to the Coriolis effect, in which a shear wave’s polarization follows a negative  
404 cosine curve (Snieder et al., 2016; Creasy et al., in review).  $S_{\text{diff}}$  waves propagating along  
405 Earth’s rotation axis (north-south) from the event show waveform changes, mainly on the  
406 radial component (Figure 6c).  $S_{\text{diff}}$  waves propagating nearly east-west (that is, perpen-  
407 dicular to Earth’s rotation axis) produce waveforms for both simulations (rotating and  
408 non-rotating) that are completely identical (Figure 6d). Overall, the differences in wave-  
409 form shapes between the two simulations for the north-south path is small (the amplitudes  
410 of the radial component must be doubled to visualize the effect; Figure 6). The polarization  
411 change due to Earth’s rotation is only  $1 - 3^\circ$  for  $S_{\text{diff}}$  waves, which is generally insignif-  
412 icant considering that error estimates on fast polarization directions are usually at least  
413  $\pm(10 - 15^\circ)$  for splitting measurements (e.g., Long and Silver, 2009). Furthermore, the  
414 pattern of polarization anomalies can be easily predicted using a raytracing approach and  
415 the effect of Coriolis-induced polarization anomalies can be corrected. Other waves such as  
416 direct S are more strongly affected by Earth’s rotation, with polarization anomalies up to  
417 almost  $7^\circ$  (Creasy et al., in review).

#### 418 4. Anisotropic effects on $\text{SH}_{\text{diff}}$ waveforms

##### 419 4.1. Influence of lowermost mantle anisotropy on $S_{\text{diff}}$ amplitudes

420 We now focus on the influence that lowermost mantle anisotropy has on  $\text{SH}_{\text{diff}}$  and  $\text{SV}_{\text{diff}}$   
421 amplitudes for initially SH-polarized  $S_{\text{diff}}$  waves. To do so, we run simulations for a model  
422 that replaces the bottom 150 km of the mantle of our initial isotropic PREM input model  
423 with Ppv anisotropy, as described in Section 2.1, initially using a global layer of anisotropy.  
424 The raypath of  $S_{\text{diff}}$  along the CMB can be very long; therefore, we also investigate how the  
425 anisotropic signature is influenced by laterally heterogeneous seismic anisotropy, by running  
426 models with finite anisotropic regions.

427 We perform simulations for three different cases. First, we incorporate a global layer  
428 of Ppv anisotropy at the base of the mantle (first row in Figure 7); then, we incorporate  
429 Ppv anisotropy in the lowermost mantle up to a distance of  $65^\circ$  from the source (second  
430 row); third, we incorporate Ppv anisotropy for epicentral distances greater than  $65^\circ$  from  
431 the source (third row). For the first case (Figure 7, first row), for which the anisotropic  
432 layer is global,  $\text{SH}_{\text{diff}}$  is clearly split, with  $\text{SV}_{\text{diff}}$  energy for the whole distance range. We  
433 also observe that for this first case,  $\text{SH}_{\text{diff}}$  and  $\text{SV}_{\text{diff}}$  amplitudes decrease similarly as a  
434 function of distance, meaning that the relative amount of energy split to  $\text{SV}_{\text{diff}}$  will reflect  
435 the lowermost mantle anisotropy, independent of the size of the anisotropic region. In the  
436 second case (Figure 7, second row), we observe splitting (with some energy partitioned  
437 to  $\text{SV}_{\text{diff}}$ ) at closer distances ( $< 115^\circ$ ), because lowermost mantle anisotropy is only being  
438 sampled at the beginning of the raypath along the CMB.  $\text{SV}_{\text{diff}}$  energy then decreases quickly  
439 as a function of distance and has largely died off at an epicentral distance of  $130^\circ$ , relative  
440 to  $\text{SH}_{\text{diff}}$ . For the third scenario (Figure 7, third row), at close distances  $S_{\text{diff}}$  waves do not  
441 sample seismic anisotropy along the CMB but do sample anisotropy after they leave the  
442 CMB on their (long) path through the  $D''$  layer. At slightly larger distances ( $\sim 115^\circ$ ), they  
443 start sampling the anisotropy along the CMB, leading to significant splitting.

444 These results have some important implications regarding  $\text{SH}_{\text{diff}}$  splitting measurements  
445 performed on real data. In the absence of upper mantle anisotropy, our simulations demon-  
446 strate the following:

- 447 • Seismic anisotropy in the lowermost mantle generally leads to splitting of energy from  
448 SH to SV for initially SH-polarized  $S_{\text{diff}}$  waves. (For the real Earth, recognizing split-  
449 ting in record sections will not be as straightforward as in Figure 7 because  $\text{SV}_{\text{diff}}$   
450 energy may not have originated from splitting, but may instead be due to the initial  
451 source polarization, as discussed in Section 3).
- 452 • Relatedly, if waveforms similar to those predicted for cases one and two (Figure 7; with  
453  $D''$  anisotropy sampled in the beginning of the raypath, or along the whole raypath)

454 were observed in real data, radial energy could not directly be attributed to splitting  
455 due to lowermost mantle anisotropy without considering the source mechanism. The  
456 possibility of  $SV_{\text{diff}}$  energy due to effects other than anisotropy can only be excluded  
457 if the focal mechanism, and therefore the amount of initial SV energy, is known.

458 • Assuming that it can be shown (via knowledge of the focal mechanism and/or wavefield  
459 simulations) that observations of significant SV energy would not be expected in the  
460 absence of lowermost mantle anisotropy, deep mantle anisotropy must be present.  $S_{\text{diff}}$   
461 splitting serves as a straightforward diagnostic of lowermost mantle anisotropy in this  
462 case. However, it will likely be challenging to infer exactly where along the raypath  
463 lowermost mantle anisotropy is present or what the lateral extent of the anisotropic  
464 region is.

465 • Only for the case shown in the third row of Figure 7, for which  $S_{\text{diff}}$  waves are not  
466 sampling  $D''$  anisotropy at close distances, and therefore there is an increase in  $SV_{\text{diff}}$   
467 amplitudes as a function of distance, can lowermost mantle anisotropy be diagnosed  
468 without knowledge of the focal mechanism. An increase of radial amplitudes as a  
469 function of distance while transverse amplitudes are decreasing (without any enigmatic  
470 waveform effects) almost certainly reflects the presence of lowermost mantle anisotropy  
471 (see waveform behavior in Section 3). Additionally, for this case, it should also be  
472 possible to localize the anisotropy by identifying which  $S_{\text{diff}}$  raypaths are associated  
473 with an increase of  $SV_{\text{diff}}$  amplitudes as a function of distance.

474 In addition to isotropic PREM, we also incorporate the 3D tomography model GyPSuM  
475 in the mantle (replacing PREM at those depths) and repeat the simulations described above,  
476 incorporating lowermost mantle anisotropy. The results are shown in Supplementary Figure  
477 S4. Apart from the arrival times of the  $S_{\text{diff}}$  waves and some minor effects to the waveforms,  
478 the general amplitude trends are the same as in as in Figure 7, so our conclusions do not  
479 depend on the details of long-wavelength mantle heterogeneity.

#### 480 4.2. Influence of source-side anisotropy on $SH_{\text{diff}}$ splitting estimates

481 We have already shown that, if there is a non-negligible initial  $SV_{\text{diff}}$  component,  $SV_{\text{diff}}$   
482 energy could potentially mimic splitting, even if no anisotropy is present. However, even if  
483 the focal mechanism is known and it can be shown that  $S_{\text{diff}}$  should be (almost) fully SH  
484 polarized,  $S_{\text{diff}}$  may sample seismic anisotropy in the upper- or mid-mantle on the source  
485 side, leading to more SV energy than would be expected for the isotropic case. Here, we  
486 investigate how anisotropy near the seismic source can affect estimates of splitting due to  
487 lowermost mantle anisotropy.

488 We first incorporate a 200 km thick anisotropic layer in the upper mantle just beneath the  
 489 source, with no anisotropy in the lowermost mantle, and investigate the cases of moderate  
 490 (2% anisotropic strength) and relatively strong (4%) upper mantle source-side anisotropy.  
 491 For the case of strong HTI upper mantle anisotropy on the source side (and no anisotropy on  
 492 the receiver side), direct S waves accumulate a time delay of  $\sim 1.8$  s for an epicentral distance  
 493 of  $60^\circ$ , which we determined by running synthetic simulations and measuring the resulting  
 494 shear wave splitting. The time delay is about half as large for the moderate splitting case.  
 495 (In general, we would expect splitting of  $S_{\text{diff}}$  waves to be weaker than for S, because SV  
 496 energy will be lost to the core upon diffraction of these waves.) In order to characterize  
 497 and quantify splitting of  $S_{\text{diff}}$  waves due to source-side anisotropy, we calculate synthetic  
 498 seismograms using AxiSEM3D for the range of (isotropic) lowermost mantle properties that  
 499 were investigated in Section 3.1, and also incorporate the GyPSuM tomography model for  
 500 the mantle into our simulations. Then, we measure the splitting intensity due to source-side  
 501 anisotropy using SplitRacer.

502 Figure 8 shows the synthetic splitting intensities as a function of epicentral distance for  
 503 a moderate strength of upper mantle source-side anisotropy (200 km thick layer, 2% HTI).  
 504 We see that, largely independent of lowermost mantle properties, the contribution of source-  
 505 side anisotropy to  $S_{\text{diff}}$  splitting is quite modest and would thus unlikely be misdiagnosed as  
 506 strong lowermost mantle splitting (Figure 7). We do see absolute  $SI$ -values that are in some  
 507 cases (slightly) larger than 0.3 for distances that are smaller than  $115^\circ$ ; in particular, for  
 508 the GyPSuM and the linear gradient scenario with a lowermost mantle velocity of  $7.5 \frac{\text{km}}{\text{s}}$ ,  
 509 the absolute  $SI$ -values exceed 0.3 in a few cases. In general, however, moderate source-  
 510 side anisotropy would not be enough to produce significant splitting in  $S_{\text{diff}}$  seismograms.  
 511 Therefore, it is not likely be mistaken for lowermost mantle anisotropy..

512 For the strong source-side anisotropy case, the results are more complicated, as shown  
 513 in Supplementary Figure S5: For the case of low  $Q_\mu$  ( $= 75$ ) and for lowermost mantle  
 514 velocities that are lower than PREM ( $-2\%$ ), the splitting contribution from the source side  
 515 can propagate through to the receiver and potentially be mistaken for lowermost mantle  
 516 splitting; for all other investigated scenarios, absolute source-side splitting intensities are  
 517 mostly lower than 0.3. Another general observation is that the influence of source-side  
 518 anisotropy tends to decrease with increasing distance (because  $SV_{\text{diff}}$  dies off faster than  
 519  $SH_{\text{diff}}$ ). Despite this, however, our results indicate that for regions with strong source-  
 520 side anisotropy,  $S_{\text{diff}}$  waves should be corrected for this contribution to reliably measure  
 521 lowermost mantle splitting. The source-side contribution can, for example, be investigated  
 522 using other waves such as direct S (e.g., Russo et al., 2010; Foley and Long, 2011; Mohiuddin  
 523 et al., 2015).

524 Our observation that strong source-side anisotropy can cause  $S_{\text{diff}}$  splitting if lowermost  
525 mantle velocities are lower than PREM (Figure 8b) poses the question of whether ULVZs can  
526 potentially have an even larger effect. In order to investigate their effects, we incorporate a  
527 global 20 km thick layer of reduced velocities into our input model. Because we expect results  
528 to depend on how much the shear-wave velocity is reduced, we conduct multiple simulations  
529 for different S wave velocity reductions. Because the results are generally very similar  
530 for different shear velocity reductions, we show the two endmembers with 2% and 20%  
531 velocity reduction in Figure 9. (We reduce P velocities by 1/3 of the value for S velocities  
532 and keep density unchanged.) Trade-offs between velocity reduction and thickness of the  
533 anisotropic layer likely exist, but are not explicitly explored here. We find that only a couple  
534 of measurements at small distances are (slightly) split, while all other measurements are null,  
535 indicating that source-side upper mantle anisotropy would not generally be mistaken for a  
536 lowermost mantle contribution if thin low velocity anomalies are present at the CMB. We  
537 conducted similar simulations for different velocity reduction percentages, which confirm  
538 this impression (Figure S6).

#### 539 *4.3. Influence of lowermost mantle anisotropy on $SH_{\text{diff}}$ splitting measurements*

540 We have shown in Section 4.1 how SV amplitudes behave as a function of distance in  
541 the presence of lowermost mantle anisotropy. Further, we have shown that strong source-  
542 side anisotropy can potentially cause  $S_{\text{diff}}$  splitting and can thus potentially be mistaken  
543 for a lowermost mantle anisotropy contribution in some cases if not properly accounted for  
544 (Section 4.2). Here, we go one step further and explicitly measure shear wave splitting  
545 (via the splitting intensity) for scenarios that include lowermost mantle anisotropy. We  
546 also investigate whether and how the presence of source-side anisotropy affects estimates of  
547 splitting parameters due to lowermost mantle anisotropy.

548 For this purpose, we compute synthetic seismograms for multiple scenarios. As in Sec-  
549 tion 4.1, we investigate how splitting measurements on initially SH-polarized  $S_{\text{diff}}$  waves  
550 are influenced by anisotropy located at different regions along the raypath. We incorporate  
551 Ppv lowermost mantle anisotropy in the mantle either for a global anisotropic layer in the  
552 lowermost mantle, for epicentral distances larger than  $65^\circ$  (measured from the source), or  
553 less than  $65^\circ$ . In order to achieve realistic splitting intensity values for these models, the  
554 anisotropic strength of the Ppv elastic tensor for the deep mantle is reduced, as described  
555 in Section 2.1. We use two different background models for these synthetics: a) isotropic  
556 PREM or b) isotropic PREM, but with the mantle structure replaced by the GyPSuM to-  
557 mography model. For each of these cases, we investigate how the addition of upper mantle  
558 anisotropy influences the shear wave splitting measurements.

559 We show results for moderately strong HTI anisotropy in the upper mantle in Figure 10.

560 We observe that splitting intensities are relatively constant as a function of distance for a  
561 full global anisotropic layer, while they either increase or decrease with epicentral distance  
562 for the two other cases. The incorporation of (isotropic) 3D heterogeneity via the GyPSuM  
563 tomography model has only a slight influence on the measured splitting intensities compared  
564 to isotropic PREM. Also, we find that moderate source-side anisotropy does not strongly  
565 affect the measured splitting. This is generally also true for strong source-side anisotropy  
566 (Supplementary Figure S7), although the strong upper mantle anisotropy has a slightly  
567 larger influence, as expected (see Section 4.2). Compared to a moderate upper mantle  
568 anisotropy strength, the 95% confidence intervals of the splitting measurements tend to  
569 become larger for strong upper mantle anisotropy.

570 From the simulations that include lowermost mantle anisotropy, we infer that even strong  
571 source-side anisotropy likely only has minor effects on the measured overall splitting if the  
572 lowermost mantle anisotropy is sufficiently strong. Because it is difficult to ensure that  
573 this condition is met, however, we nevertheless recommend only using data that does not  
574 sample strong anisotropy in the source side upper mantle, which can be assured using data  
575 from phases other than  $S_{\text{diff}}$ . Moreover, we have demonstrated that including realistic 3D  
576 heterogeneity does not have a large effect on the measured  $S_{\text{diff}}$  splitting parameters.

## 577 **5. Discussion**

### 578 *5.1. Strategy for $S_{\text{diff}}$ splitting measurements*

579 We have argued that in order to avoid introducing large uncertainties, splitting should  
580 only be measured on  $S_{\text{diff}}$  waves that have a negligible initial  $SV_{\text{diff}}$  component. We have  
581 shown in Section 3.1 that the assumption that  $SV_{\text{diff}}$  has died off at any particular distance,  
582 and therefore that all SV energy is due to splitting, cannot be made universally. However,  
583 there are some examples for which this assumption is indeed appropriate. Specifically,  
584 when  $S_{\text{diff}}$  waves sample regions in which the lowermost mantle velocity is greater than  
585 average and for certain attenuation structures,  $SV_{\text{diff}}$  waves are predicted to die off quickly  
586 compared to  $SH_{\text{diff}}$ . There is, however, substantial uncertainty regarding lowermost mantle  
587 properties, which makes it difficult to ensure that these conditions are met for any source-  
588 receiver pair. If isotropic lowermost mantle conditions and  $S_{\text{diff}}$  initial polarization are  
589 known perfectly, seismic anisotropy could be characterized if  $S_{\text{diff}}$  has a mixed  $SH_{\text{diff}}$  versus  
590  $SV_{\text{diff}}$  initial polarization, for example through a waveform modeling approach. However,  
591 in practice, there is significant uncertainty about the detailed properties of the lowermost  
592 mantle. Therefore, we suggest to ensure that  $S_{\text{diff}}$  is primarily SH polarized via knowledge  
593 of the focal mechanism. Before measuring  $S_{\text{diff}}$  splitting, it should be verified that for the  
594 selected source-receiver configuration, little or no  $SV_{\text{diff}}$  energy can be expected to arrive at

595 the receiver in an isotropic Earth. This evaluation can be done by using full-wave simulations  
596 (by incorporating the known moment tensor), as we do here, or by calculating the initial  
597 polarization based on the moment tensor. These simulations can and should consider a  
598 priori information about the velocity and attenuation structure of the particular region. It  
599 may not be sufficient to rely on isotropic PREM to investigate whether negligible  $SV_{\text{diff}}$   
600 energy can be expected, particularly if raypaths sample structures such as LLVPs or regions  
601 with higher than average velocities.

602 We have also shown in Section 4 that, even for cases in which  $S_{\text{diff}}$  would be primarily  
603 SH polarized in an isotropic Earth, splitting can occur in the upper mantle on the source  
604 side, which can potentially be misinterpreted as evidence of lowermost mantle anisotropy if  
605 one does not account for this possibility. Events associated with regions of strong source-  
606 side anisotropy can be avoided by explicitly measuring source-side splitting using direct  
607 S or by focusing on particularly deep events (i.e.,  $> 400$  km). While the uppermost lower  
608 mantle and the transition zone have been shown to be anisotropic in some cases, particularly  
609 in subduction zone settings, they generally produce splitting with delay times  $< 1$  s (e.g.,  
610 Foley and Long, 2011; Lynner and Long, 2015; Mohiuddin et al., 2015). This means that  
611 deep events ( $> 400$  km) can generally be used for  $S_{\text{diff}}$  splitting measurements because only  
612 relatively weak source-side splitting ( $\delta t < 1$  s) can be expected for them. In any case, it  
613 must be ensured in  $S_{\text{diff}}$  splitting analyses that candidate  $SH_{\text{diff}}$  waves sample only weak to  
614 moderate source-side anisotropy.

615 Apart from potentially sampling source-side and lowermost mantle anisotropy,  $S_{\text{diff}}$  waves  
616 will generally also be affected by anisotropy in the receiver-side upper mantle (and perhaps  
617 the crust), just like other waves used to study the deep mantle. A feasible approach to  
618 characterize upper mantle anisotropy beneath stations is to measure SKS splitting over a  
619 range of backazimuths, as SKS waves generally reflect contributions from the upper mantle  
620 beneath the receiver in most cases (e.g., Becker et al., 2015).  $S_{\text{diff}}$  waves can then be  
621 explicitly corrected for this contribution before measuring  $D''$ -associated splitting. Such an  
622 approach has been shown to accurately retrieve the fast polarization direction,  $\phi$ , for direct  
623 source side S splitting; uncertainties of  $\delta t$  measurements are large, however (Wolf et al.,  
624 2022a). While explicit receiver side corrections are the most straightforward way to account  
625 for account for upper mantle anisotropy beneath the receiver, there may also be alternative  
626 strategies, particularly in cases where array data are available. (We will discuss alternatives  
627 in Section 5.3.) In any case, it should be demonstrated that any measured  $S_{\text{diff}}$  splitting  
628 signature cannot be explained by receiver side upper mantle anisotropy, and explicit receiver  
629 side corrections are often appropriate. In some cases, it may only be possible to demonstrate  
630 that  $S_{\text{diff}}$  is affected by lowermost mantle anisotropy, without the ability to explicitly measure

631 the lowermost mantle associated splitting parameters (due to uncertainties associated with  
632 receiver-side corrections).

633 After measuring the lowermost mantle-associated splitting parameters, it should be con-  
634 sidered that there is significant uncertainty regarding where along the  $S_{\text{diff}}$  raypath splitting  
635 has occurred. In general, anisotropy sampled earlier along the  $D''$  portion of the ray's path  
636 will affect the measured splitting parameters at the station less than anisotropy that is  
637 sampled later on the raypath (Section 4.1), due to full-wave effects. A single measurement,  
638 however, does not suffice to show where exactly seismic anisotropy is present in the low-  
639 ermost mantle. Inferences on the likely distribution of anisotropy may be possible when  
640 multiple measurements from dense seismic arrays are interpreted together; furthermore, an-  
641 isotropy may be localized by taking advantage of crossing raypaths (e.g., Nowacki et al.,  
642 2010; Ford et al., 2015; Creasy et al., 2021). We also point out that the measured splitting  
643 at the receiver will be affected by a large  $D''$  volume, as the sensitivity kernels for  $S_{\text{diff}}$  waves  
644 at the base of the mantle are broad.

645 To summarize, our suggested workflow for  $S_{\text{diff}}$  splitting measurements to detect lower-  
646 most mantle anisotropy includes the following steps:

- 647 1. Ensure that  $S_{\text{diff}}$  can be expected to be almost fully  $SH_{\text{diff}}$  polarized in an isotropic  
648 Earth for the raypaths under study. This can, for example, be done via full-wave  
649 simulations.
- 650 2. Exclude a substantial source-side upper mantle contribution, either by characterizing  
651 the source-side anisotropy through other phases (e.g., direct S) or by focusing on deep  
652 earthquakes ( $> 400$  km).
- 653 3. Measure  $S_{\text{diff}}$  splitting parameters using standard techniques.
- 654 4. If necessary, explicitly correct for receiver side upper mantle anisotropy.
- 655 5. Interpret  $S_{\text{diff}}$  splitting measurements in terms of lowermost mantle anisotropy, con-  
656 sidering that it is often unclear where exactly along the raypath lowermost mantle  
657 anisotropy was sampled.

## 658 5.2. $S_{\text{diff}}$ splitting strategy in light of previous work

659 Previous work investigated apparent time delays between  $SH_{\text{diff}}$  and  $SV_{\text{diff}}$  for simple  
660 Earth models (Komatitsch et al., 2010), different mantle attenuation structure (Borgeaud  
661 et al., 2016), and realistic 3D velocity structure (Parisi et al., 2018). In these studies, events  
662 were chosen such that  $S_{\text{diff}}$  waves are partially SH and partially SV polarized, with both com-  
663 ponents generally having a similar amplitude. The radial energy that produced differential  
664  $SH_{\text{diff}}$ - $SV_{\text{diff}}$  travel times in absence of seismic anisotropy in previous studies (Komatitsch

665 et al., 2010; Borgeaud et al., 2016; Parisi et al., 2018) was mostly due to initial SV energy  
 666 propagating along the CMB. In practice, however,  $S_{\text{diff}}$  phases are often primarily SH polar-  
 667 ized. We have suggested in this study that  $S_{\text{diff}}$  waves can be used for splitting measurements  
 668 for cases in which  $SH_{\text{diff}}$  can be expected to be much larger than  $SV_{\text{diff}}$ , thereby excluding  
 669 effects similar to those reported in previous papers. Additionally, instead of focusing on  
 670 differential  $SH_{\text{diff}}-SV_{\text{diff}}$  travel times which often result from waveform distortions, we have  
 671 explicitly measured splitting parameters ( $\phi$ ,  $\delta t$ ;  $SI$ ) in our study. This approach helps avoid  
 672 the misinterpretation of  $SV_{\text{diff}}$  energy that results from isotropic structure (for example,  
 673 due to the presence of ULVZs or phase interference) as splitting. The reason for this is that  
 674 well-constrained splitting parameters will only be obtained (for an initially SH-polarized  
 675  $S_{\text{diff}}$  phase) if the radial component has a similar shape as the transverse component time  
 676 derivative. To summarize, previous studies have analyzed differential  $SH_{\text{diff}}-SV_{\text{diff}}$  travel  
 677 times from partially SH and SV-polarized  $S_{\text{diff}}$  waves. We measure splitting parameters for  
 678  $S_{\text{diff}}$  waves that can be assumed to initially be SH-polarized, a different approach than that  
 679 taken in this work. The results from this study, including our suggested splitting strategy,  
 680 are fully consistent with the previous findings of Komatitsch et al. (2010), Borgeaud et al.  
 681 (2016) and Parisi et al. (2018).

### 682 5.3. Real data example

683 In order to illustrate our suggested  $S_{\text{diff}}$  splitting strategy, we present a real data example  
 684 using EarthScope USArray data from North America. We focus on a source-receiver geome-  
 685 try for which  $S_{\text{diff}}$  splitting has been identified previously (Wolf and Long, 2022) but expand  
 686 our analysis to consider additional earthquakes. We use three events that occurred in 2009  
 687 and 2010 beneath the Celebes Sea; at this time, a large number of USArray Transportable  
 688 Array stations were deployed at an epicentral distance range of  $101^\circ$  to  $120^\circ$ . Figure 11a  
 689 illustrates our source-receiver geometry sampling the lowermost mantle beneath the north-  
 690 ern Pacific Ocean, where we highlight the sections of the raypath along the CMB. The  
 691 station selection for all three events is very similar (but not identical, because we discard  
 692 low-quality data from some stations and because the events occurred at different times).  
 693 The substantial overlap also means that the raypaths are similar for all three events.

#### 694 *Step 1: Initial polarization of $S_{\text{diff}}$*

695 As a first step, following the strategy laid out in Section 5.1, we investigate the expected  
 696  $S_{\text{diff}}$  polarizations for each event. We obtain the focal mechanisms of all three events from the  
 697 USGS database and conduct synthetic simulations using AxiSEM3D (for the same source-  
 698 receiver configurations as for the real data). The background velocity model that we use  
 699 is isotropic PREM, but we replace the velocities in the lowermost mantle with velocities

700 from a (isotropic) local 3-D shear wave velocity model beneath the northern Pacific Ocean  
701 (Suzuki et al., 2021) to approximate the local velocity structure. We incorporate the Suzuki  
702 et al. (2021) model rather than a global model here because it represents smaller scale  
703 velocity heterogeneity in the lowermost mantle of our study region. We do not incorporate  
704 ULVZs because we have shown before that SV energy due to ULVZs is unlikely to mimic  
705 splitting (Section 3.2), and because no ULVZs have been unambiguously identified in our  
706 region of interest (Yu and Garnero, 2018). The synthetic radial and transverse component  
707 seismograms for three simulations are shown in Figure 11c-e. Fortunately, for all three  
708 events, little or no  $SV_{\text{diff}}$  energy would be expected in an isotropic Earth, although predicted  
709  $SV_{\text{diff}}$  amplitudes for event 2009-10-07 are slightly larger than for the other two events.  
710 Despite that, these modeling results indicate that  $S_{\text{diff}}$  splitting analyses can be conducted  
711 for all three events, as any significant SV energy can be attributed to splitting behavior and  
712 not isotropic structure.

713 *Step 2: Influence of source-side anisotropy*

714 Second, we investigate the possibility of source-side anisotropy contributions to our wave-  
715 forms. All the three events used in this study occurred at depths greater than 580 km. As  
716 argued in Section 4.3 and Section 5.1, significant source-side anisotropy (with delay times  
717  $> 1$  s) is unlikely for such deep events (e.g., Foley and Long, 2011; Lynner and Long, 2015).  
718 This was also explicitly shown by Mohiuddin et al. (2015) for the Celebes Sea, where the  
719 three earthquakes under study occurred.

720 *Step 3:  $S_{\text{diff}}$  splitting due to lowermost mantle anisotropy*

721 Next, we investigate whether the  $S_{\text{diff}}$  waves from our three events show any evidence  
722 of lowermost mantle anisotropy. We focus on a subset of the data that shows convincing  
723 evidence for  $SV_{\text{diff}}$  energy due to  $D''$ -associated splitting at azimuths  $> 43^\circ$  and distances  
724  $> 110^\circ$  for all three events (Figure 12), building upon work from Wolf and Long (2022).  
725 In Wolf and Long (2022), a similar subset of  $S_{\text{diff}}$  data for event 2010-10-07 was analyzed,  
726 in combination with measurements of differential SKS-SKKS splitting. In that previous  
727 work, we mainly based our interpretation in that work on SKS-SKKS differential splitting  
728 results. With the results presented in this paper, we can now be fully confident that the  
729 observed  $SV_{\text{diff}}$  energy indeed reflects splitting due to deep mantle anisotropy. Here, we  
730 extend our analysis to two additional events and measure  $S_{\text{diff}}$  splitting due to lowermost  
731 mantle anisotropy for all three earthquakes.

732 *Step 4: Receiver-side anisotropy contribution*

733 Figure 12 shows  $S_{\text{diff}}$  waveforms for all three events aligned via cross-correlation of the  
734 transverse components. Energy is clearly split to the radial component for all events; in fact,

735 the stacked waveforms (black lines; Figure 12) look very similar for all three earthquakes.  
736 Figure 13a-c is similar to Figure 12 (for the same source-receiver pairs) but for SKS waves.  
737 Figure 13 demonstrates that the splitting of energy from the transverse to the radial compo-  
738 nent of  $S_{\text{diff}}$  for these events cannot be explained by the presence of upper mantle anisotropy  
739 beneath the receiver only. This conclusion can be made because no strong, coherent splitting  
740 of energy from the radial to the transverse components can be observed for SKS, suggesting  
741 that the upper mantle anisotropy beneath the receivers generally causes relatively weak and  
742 incoherent splitting for this event. This in turn implies that differences in splitting between  
743  $S_{\text{diff}}$  and SKS originate from contributions to  $S_{\text{diff}}$  splitting from anisotropy along the por-  
744 tion of the raypath through the lowermost mantle. This result is not entirely surprising,  
745 considering that the upper mantle splitting pattern from the IRIS splitting database (IRIS  
746 DMC, 2012) shows relatively weak and variable splitting across the array (Figure 13d). We  
747 infer from this exercise that for the  $S_{\text{diff}}$  waves (measured and stacked across the same set  
748 of stations as SKS) the receiver side upper mantle contribution can be expected to largely  
749 average out as well.

750 We next quantitatively investigate the degree to which the waveforms are influenced by  
751 lowermost vs. upper mantle anisotropy by measuring SKS and  $S_{\text{diff}}$  splitting intensities for all  
752 individual seismograms from our three events (recorded at the stations shown in Figure 11).  
753 We compare these two phases because differences between SKS and  $S_{\text{diff}}$  splitting likely  
754 reflect a contribution from  $D''$ , as argued above. Furthermore, we have previously shown  
755 that for this source-receiver geometry, SKS is likely primarily influenced by receiver side  
756 upper mantle anisotropy (Wolf and Long, 2022).

757 Our measurements of SKS and  $S_{\text{diff}}$  splitting intensities for individual seismograms are  
758 shown in Figure 14 as a function of epicentral distance from the source. We find that  
759 while SKS splitting intensities tend to decrease as a function of distance and scatter around  
760 zero for distances that are larger than  $110^\circ$ ,  $S_{\text{diff}}$  waves for all three events, in contrast,  
761 consistently show a pronounced increase in splitting intensities at an epicentral distance  
762 of approximately  $110^\circ$ . This increase occurs at slightly larger distances for event 2009-10-  
763 07; this event occurred slightly farther away from the USArray stations than the other two  
764 events (Figure 11a).  $S_{\text{diff}}$  splitting intensities plateau for distances  $> 110^\circ$  (Figure 14). Thus,  
765 the anisotropic signature apparently does not change as a function of distance, indicating  
766 that  $S_{\text{diff}}$  is likely sampling a large, uniformly anisotropic region at the base of the mantle.  
767 This is also supported by the observation of coherent and uniform  $S_{\text{diff}}$  splitting in the  
768 record sections that show the waveforms for these distances (Figure 12). The observation  
769 that SKS splitting intensities scatter around zero for distances from  $110^\circ$  to  $120^\circ$  indicates  
770 the presence of generally fairly weak upper mantle anisotropy that varies laterally across

771 the area in which the receivers are positioned. This is consistent with previously published  
772 estimates of SKS splitting at these stations (Figure 13d). In contrast to SKS splitting,  
773  $S_{\text{diff}}$  splitting is consistently very strong at epicentral distances larger than  $110^\circ$ , showing a  
774 distinctly different pattern than SKS. This indicates a considerable influence of lowermost  
775 mantle anisotropy on  $S_{\text{diff}}$  waves.

776 We emphasize that the approach we have taken here, which relies on visual inspection of  
777 record sections and measurements of splitting intensity as a function of distance, can only  
778 be used if  $S_{\text{diff}}$  waves from one event are recorded across a large seismic array. Without such  
779 a favorable source-receiver configuration, patterns of splitting intensity with distance could  
780 not be resolved well; furthermore, if  $S_{\text{diff}}$  waves are too noisy or stations are too sparse, it  
781 may not be possible to reliably resolve trends of the splitting intensity. Additionally, this  
782 particular dataset allows us to measure splitting from single station  $S_{\text{diff}}$  data without ex-  
783 plicitly correcting for the upper mantle contribution, as discussed below; for other datasets,  
784 explicit receiver-side upper mantle corrections will generally be needed.

785 *Step 5: Interpretation of  $S_{\text{diff}}$  splitting parameters in terms of deep mantle anisotropy*

786 Our next step is to measure the lowermost mantle associated splitting parameters. To do  
787 this, we again focus on the subset of stations for which Wolf and Long (2022) demonstrated a  
788 strong lowermost mantle anisotropy contribution for event 2009-10-07. Specifically, we focus  
789 on the distances  $> 110^\circ$  and azimuths  $< 43^\circ$  and take an approach that involves stacking our  
790 data. We note that data should only be stacked over a distance and azimuth range for which  
791 a uniform lowermost mantle signature can be inferred based on the waveform behavior. In  
792 our case, the waveforms in Figure 12 indicate that splitting is uniform. Additionally, we  
793 measure  $S_{\text{diff}}$  splitting parameters of the single station  $S_{\text{diff}}$  seismograms, which yields similar  
794  $(\phi', \delta t)$  measurements over the whole distance/azimuth range of interest (Figures S8-S10),  
795 indicating that the influence of lowermost anisotropy is more dominant than the (weak)  
796 upper mantle receiver side anisotropy (Figure 13d).

797 We now focus on the  $S_{\text{diff}}$  waveforms for the epicentral distance ( $> 110^\circ$ ) and azimuth  
798 ( $< 43^\circ$ ) ranges for which a lowermost mantle contribution to splitting has been observed  
799 (and for which the corresponding SKS stack splitting is null). We align the  $S_{\text{diff}}$  waveforms  
800 by cross-correlation of the transverse components as shown in Figure 15a-b. For all three  
801 events, we observe a strong and coherent splitting signal, expressed in  $S_{\text{diff}}$  amplitudes,  
802 caused by the contribution of lowermost mantle anisotropy. In order to increase SNR and  
803 thus confidence in our measurements, in addition to measuring splitting intensities for in-  
804 dividual seismograms (Figure 11), we also stack the  $S_{\text{diff}}$  waveforms across the array and  
805 measure splitting parameters  $(\phi, \delta t)$  from these  $S_{\text{diff}}$  stacks. Results for one event are shown  
806 in Figure 15, which shows the splitting diagnostic plots for event 2010-10-04. We do not

807 implement an explicit correction for the effect of the Coriolis force because we have shown  
808 that these effects are generally negligible (Section 3.3). We find that the splitting param-  
809 eters measured for each of the three events agree extremely well (see Supplementary Figures  
810 S11 and S12 for events 2010-10-07 and 2010-07-29), with a maximum difference of  $3^\circ$  for  $\phi$   
811 and 0.1 s for  $\delta t$  (the average values are  $\phi \approx 134^\circ$  and  $\delta t \approx 1.5$  s). The splitting measure-  
812 ments from the stacks agree with the single station splitting measurements for this dataset  
813 (Supplementary Figures S8-S10) but are more robust.

814 As a final step,  $S_{\text{diff}}$  splitting measurements can be interpreted in terms of lowermost  
815 mantle deformation and flow directions. This is best accomplished via a forward modeling  
816 approach; in particular, we can carry out global wavefield simulations for different lowermost  
817 mantle anisotropy scenarios and compare predictions to data. We have previously applied  
818 such an approach for event 2010-10-07 in our dataset, which was modeled simultaneously  
819 with observations of  $D''$ -associated splitting of SKKS waves (Wolf and Long, 2022). Our  
820 previous study showed that  $S_{\text{diff}}$  splitting for the source-receiver pairs examined in this study  
821 can be explained with a model that invokes lattice-preferred orientation of Ppv resulting  
822 from slab-driven flow in the lowermost mantle beneath the northeastern Pacific Ocean.  
823 Although we used only one event from that study to conduct  $S_{\text{diff}}$  splitting measurements,  
824 the results from all three events examined here are highly consistent with the results from  
825 Wolf and Long (2022). Thus, the three measurements can also be explained by the same  
826 deformation scenario.

#### 827 5.4. $S_{\text{diff}}$ splitting analyses on single-station data: Limitations and ways forward

828 One main advantage with the array data used in Section 5.3 is that the upper mantle  
829 splitting contribution is such that explicit anisotropy corrections for the upper mantle on  
830 the receiver side are not needed. In many or most cases, however, explicit corrections for  
831 upper mantle anisotropy may need to be applied. Even in such cases, however, it may be  
832 useful to stack data to improve signal-to-noise ratios. Apart from the approach used here,  
833 there are various other strategies to account for the influence of receiver side anisotropy on  
834  $S_{\text{diff}}$  waves. A common approach is to measure SKS splitting for every station, preferably  
835 using multiple events from different backazimuths (e.g., Lynner and Long, 2014; Lynner and  
836 Long, 2015).  $S_{\text{diff}}$  waveforms can then be corrected for the upper mantle associated splitting  
837 parameters obtained this way. We would advise against measuring SKS splitting for a few  
838 backazimuths only because splitting beneath any particular station may be complex, and  
839 any single SKS splitting measurement may potentially be influenced by lowermost mantle  
840 anisotropy (e.g., Wolf et al., 2022a). Alternatively, a strategy to account for the  $S_{\text{diff}}$  upper  
841 mantle contribution can be to correct  $S_{\text{diff}}$  for the SKS/SKKS splitting parameters for  
842 the same source receiver configuration, if SKS and SKKS are split similarly. (If they are

843 not, at least one of the phases is likely influenced by lowermost mantle anisotropy and  
844 both measurements cannot be assumed to be due to upper mantle anisotropy only.) A  
845 major disadvantage of this strategy is that well-constrained SKS, SKKS and S<sub>diff</sub> splitting  
846 parameters would be required for the same source-receiver configuration. Finding data for  
847 which it is possible to obtain such good splitting measurements from three phases in one  
848 seismogram may be challenging. A special case of this approach is if SKS and SKKS splitting  
849 are null for the raypath under study. In this case, S<sub>diff</sub> splitting could be interpreted to be  
850 due to lowermost mantle anisotropy, and no corrections would need to be applied.

851 The investigation of S<sub>diff</sub> waves recorded across a dense, large-aperture array makes  
852 patterns of splitting more obvious than they would be for single station measurements  
853 (for example, the opposite trends of SKS and S<sub>diff</sub> splitting intensities that is shown in  
854 Figure 14). Applying our observational strategy to an S<sub>diff</sub> dataset from a relatively large  
855 array is also helpful in localizing the anisotropy. In our case, for example, we know that the  
856 S<sub>diff</sub> waves show a particularly strong signature of lowermost mantle anisotropy for distances  
857  $> 110^\circ$ . With this knowledge, the dimensions of the anisotropic region in the lowermost  
858 mantle can be (partially) inferred. In contrast, for a single S<sub>diff</sub> splitting measurement it  
859 would not possible to infer where the anisotropy is localized along the S<sub>diff</sub> raypath. Some  
860 caution is also warranted when stacking waveforms across a large array (and thus averaging  
861 anisotropy across a relatively large portion of the lowermost mantle). For our dataset this  
862 approach is justified, because splitting is coherent for the S<sub>diff</sub> waves sampling the D'' region  
863 under study (Figure 11a and Supplementary Figures S8-S10). In other cases, however,  
864 anisotropy could potentially vary laterally, yielding variability in splitting. In general, only  
865 those waveforms that show coherent splitting should be stacked, which may mean focusing  
866 on smaller distance/azimuth intervals.

## 867 **6. Conclusion**

868 In this work, we have investigated isotropic and anisotropic effects on S<sub>diff</sub> polarizations  
869 in order to understand whether and how the splitting of S<sub>diff</sub> waves can be used to infer low-  
870 ermost mantle anisotropy. We have used full-wave simulations to demonstrate, for a range  
871 of isotropic mantle models, that SV<sub>diff</sub> amplitudes do not necessarily decrease substantially  
872 faster as function of distance than SH<sub>diff</sub> amplitudes. Thus, only S<sub>diff</sub> waves with a negligible  
873 initial SV component should be used to conduct D'' shear wave splitting measurements, and  
874 care must be taken to select suitable events for analysis. In order to evaluate the effects  
875 of upper and mid-mantle anisotropy on S<sub>diff</sub> splitting, we tested models with anisotropy  
876 near the source and found that weak or moderate source-side splitting ( $\delta t_{source} < 1$  s) has  
877 minimal effects on S<sub>diff</sub> waves in most models. However, strong source-side anisotropy can

878 cause  $S_{\text{diff}}$  splitting and should be avoided in lowermost mantle anisotropy studies. We have  
879 further shown that lowermost mantle anisotropy can be recognized by strong splitting of  
880 energy from  $SH_{\text{diff}}$  to  $SV_{\text{diff}}$  (for initially SH-polarized  $S_{\text{diff}}$  waves), while realistic isotropic  
881 Earth structure does not mimic such a behavior. Our simulations have demonstrated that  
882  $S_{\text{diff}}$  waves can, indeed, be used to infer lowermost mantle anisotropy under many condi-  
883 tions. These insights have helped us formulate a strategy for carrying out measurements of  
884  $S_{\text{diff}}$  splitting due to  $D''$  anisotropy. Important considerations include showing that the  $S_{\text{diff}}$   
885 waves of interest would be almost completely SH polarized in an isotropic Earth and are  
886 not influenced by strong source-side anisotropy ( $\delta t_{\text{source}} < 1$  s). To illustrate our proposed  
887 splitting strategy, we conducted a systematic  $S_{\text{diff}}$  splitting analysis for real waveforms for  
888 western Pacific earthquakes measured at USArray stations, revealing evidence for strong,  
889 coherent anisotropy in the lowermost mantle beneath the northeastern Pacific.

## 890 **Acknowledgements**

891 This work was funded by Yale University and by the U.S. National Science Foundation  
892 via grant EAR-2026917 to MDL, grant EAR-1855206 to NC, and grant EAR-1853911 to EG.  
893 We thank the Yale Center for Research Computing for providing the research computing  
894 infrastructure for this study. We are also grateful to the Extreme Science and Engineer-  
895 ing Discovery Environment (XSEDE) Texas Advanced Computing Center (TACC) at The  
896 University of Texas at Austin through allocation TG-EES200011 using XSEDE resources  
897 (Towns et al., 2014). We acknowledge the Yale seismology group for helpful discussions.  
898 The Generic Mapping Tools (Wessel and Smith, 1998), ObsPy (Beyreuther et al., 2010),  
899 MSAT (Walker and Wookey, 2012) and SplitRacer (Reiss and Rumpker, 2017) were used in  
900 this research. We are grateful to the editor, Ana Ferreira, and an anonymous reviewer for  
901 their constructive comments that helped us improve the manuscript.

## 902 **Data availability**

903 The synthetic seismograms for this study were computed using `AxiSEM3D` and `SPECFEM3D_GLOBE`,  
904 which are publicly available at <https://github.com/AxiSEMunity> and [https://geodynamics.org/cig/software/specfem3d\\_globe](https://geodynamics.org/cig/software/specfem3d_globe). All USArray data (IRIS Transportable Array, 2003)  
905 were downloaded through IRIS (<https://service.iris.edu/>).  
906

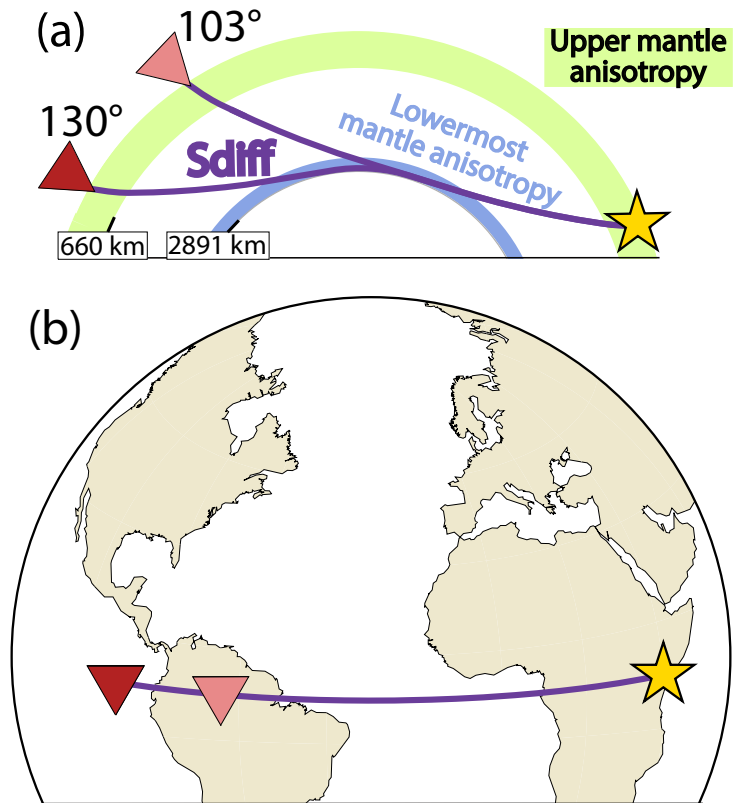


Figure 1: Schematic illustration of a typical source-receiver configuration in our numerical simulations. The  $S_{diff}$  raypath is shown by a solid purple line. (a) Cross-section through Earth. Stations are represented as red triangles and the source as a yellow star.  $S_{diff}$  potentially travels through upper mantle anisotropy at source and receiver side (green), and lowermost mantle anisotropy (blue). (b) Map view of the source, located at the equator (at longitude  $-90^\circ$ ), and the  $S_{diff}$  raypath to stations located in a distance of  $103^\circ$  and  $130^\circ$  at the equator.

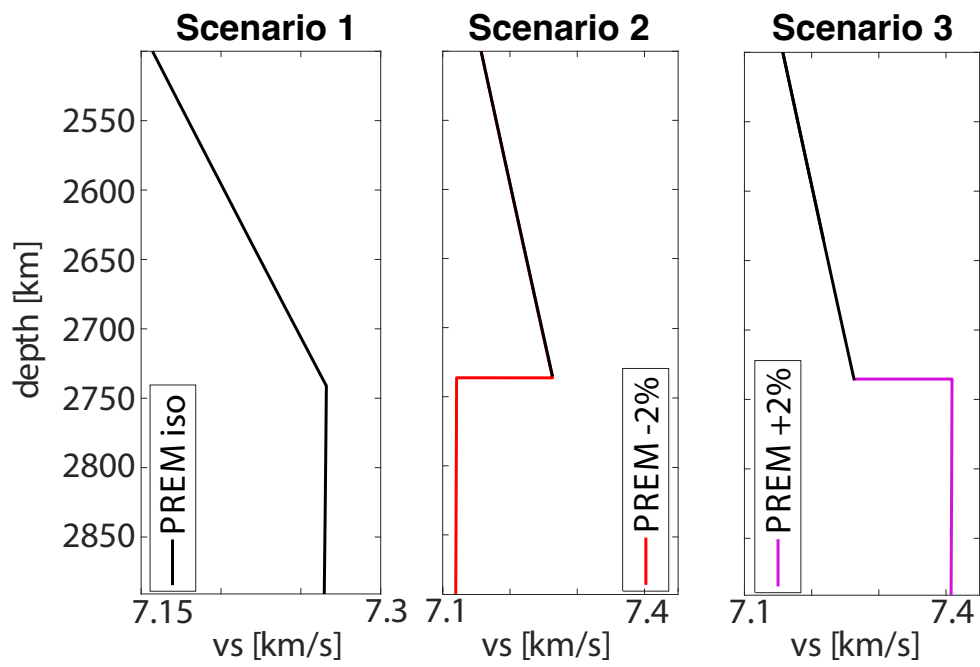


Figure 2: 1D models velocity models used in our simulations. Scenario 1: Isotropic PREM (Dziewonski and Anderson, 1981); scenario 2: Isotropic PREM, with 2% lower velocities in the lowermost 150 km of the mantle; scenario 3: Isotropic PREM, with 2% increased velocities in the lowermost 150 km of the mantle.

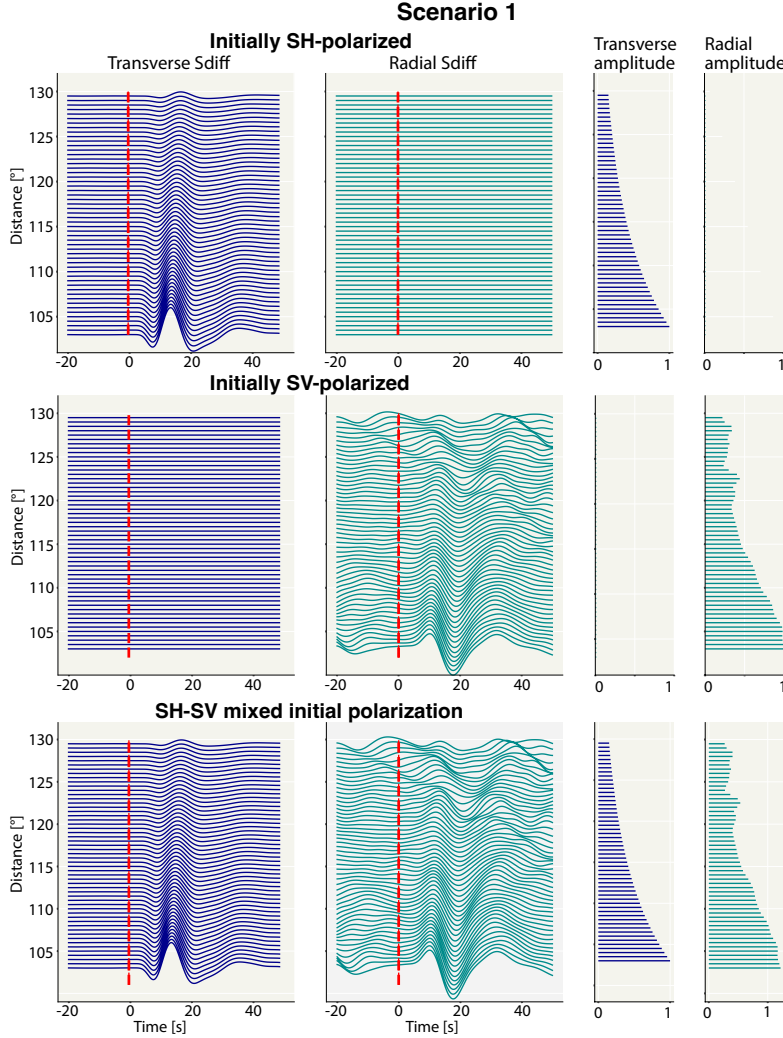


Figure 3: Displacement synthetic seismograms for simulations using PREM (Dziewonski and Anderson, 1981) as an input model (scenario 1 in Figure 2), calculated for a focal depth of 0 km. We show transverse (first column, dark blue) and radial (second column, teal)  $S_{\text{diff}}$  waveforms and corresponding transverse (third column, dark blue) and radial (fourth column, teal) amplitudes as a function of epicentral distance. The amplitudes are plotted relative to the transverse (row 1 and 3) and radial  $S_{\text{diff}}$  (row 2) amplitudes at the lowest distance and measured as the maximum absolute values in a time window of from the predicted  $S_{\text{diff}}$  arrival to 30 s after it. Three simulations are shown for SH (top row), SV (middle row) and mixed SH-SV initial polarizations (bottom row). Seismograms are shown from 20 s before the predicted  $S_{\text{diff}}$  arrival time until 60 s after. Predicted arrival times are calculated using TauP (Crotwell et al., 1999) for the PREM model (red dashed lines). Waveforms are shown after applying a 10 – 50 s bandpass filter.

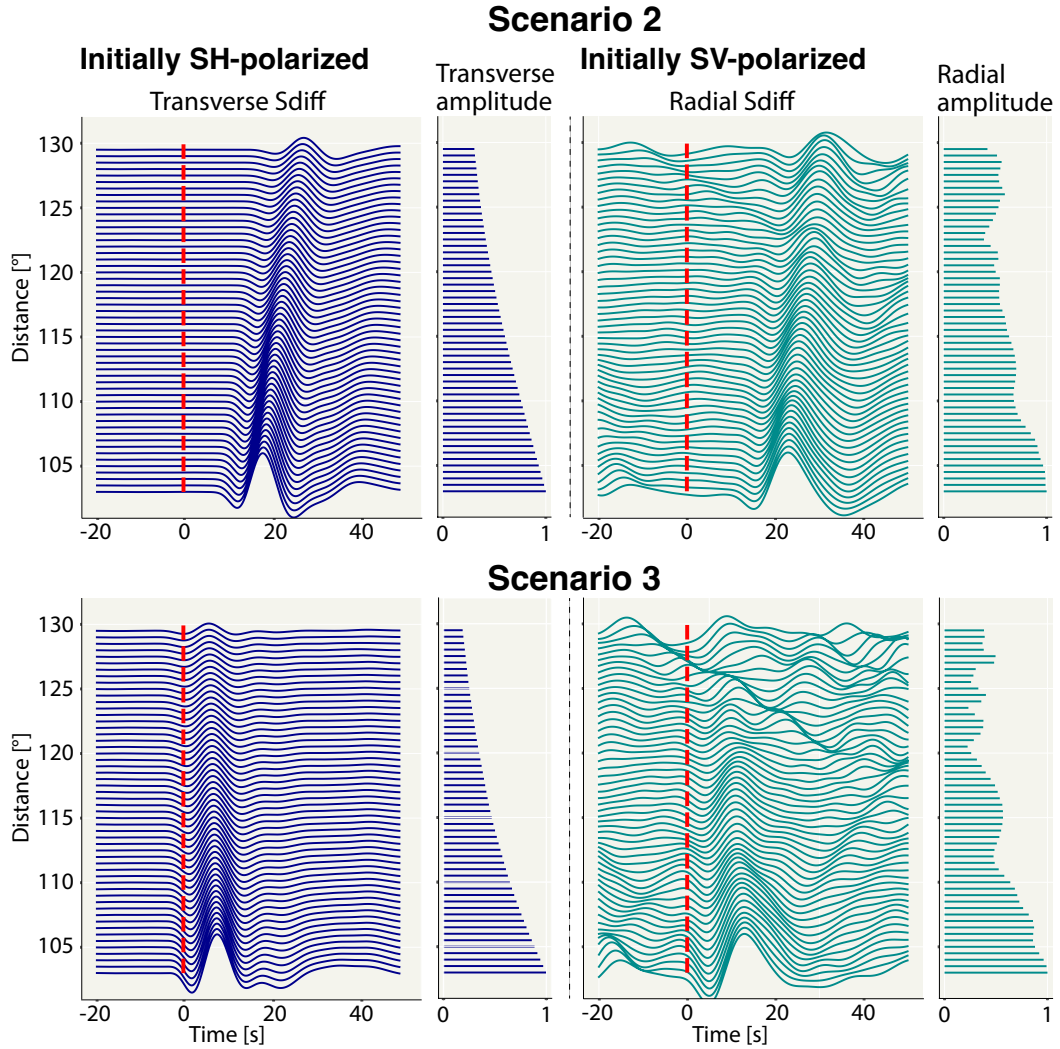


Figure 4: Transverse and radial  $S_{\text{diff}}$  displacement waveforms and amplitudes for 2% lower (scenario 2, top row) and 2% higher (scenario 3, bottom row) shear wave velocities than PREM (Dziewonski and Anderson, 1981) in the lowermost 150 km of the mantle, calculated using a focal depth of 0 km. The amplitudes are plotted relative to the  $SH_{\text{diff}}$  (column 1) and  $SV_{\text{diff}}$  (column 3) amplitudes at the closest distance. Simulations are conducted for initially fully SH (first/second column) and SV (third/fourth column) polarized  $S_{\text{diff}}$  waves. Waveforms are shown in columns 1 and 3; amplitudes are shown in columns 2 and 4. In contrast to Figure 3, only those panels are shown for which  $S_{\text{diff}}$  amplitudes are non-null. Other plotting conventions are the same as in Figure 3.

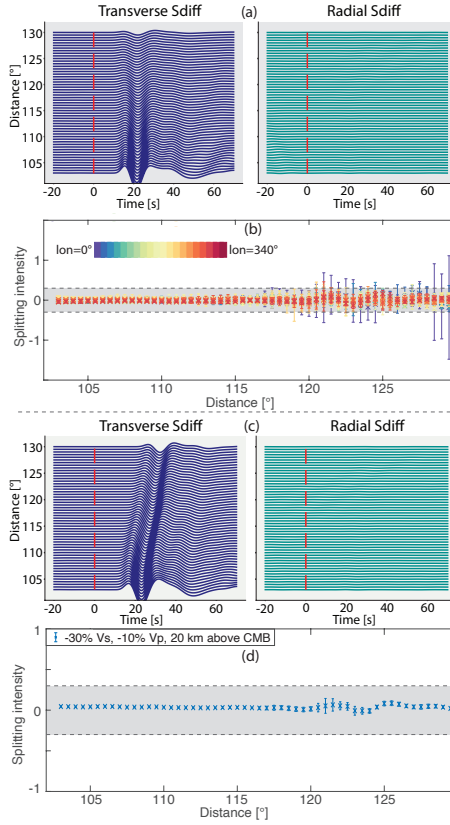


Figure 5: Results from simulations investigating isotropic effects on polarizations of (initially SH polarized)  $S_{\text{diff}}$  waves. (a) Transverse (left panel, dark blue) and radial (right panel, teal) waveforms as a function of distance for a simulation using the 3D tomography model GyPSuM (Simmons et al., 2010) for the mantle and isotropic PREM (Dziewonski and Anderson, 1981) elsewhere, calculated for a focal depth of 0 km. The amplitudes are plotted relative to the transverse  $S_{\text{diff}}$  amplitude at the lowest distance. For this simulation, the source was placed at the north pole and the receivers were positioned along  $60^\circ$  longitude. While a clear arrival is visible on the transverse component, almost no energy arrives on the radial. Red dashed lines indicate predicted arrival times according to PREM. Waveforms are shown after applying a bandpass filter between 10 – 50 s. (b) Splitting intensities, measured using SplitRacer (Reiss and Rumpker, 2017), as a function of distance for analogue source-receiver configurations as in (a), along different longitudes (with a spacing of  $20^\circ$ ; see legend). All splitting intensity measurements are null ( $|SI| < -0.3$ ; indicated by black dashed lines). (c) Results for scenarios that include a global 20 km thick basal layer with largely reduced shear velocities (see legend) are shown. S wave velocity reductions are chosen to be 30% and P wave velocity reduction to be 10% compared to PREM (see legend), which is similar to the velocity reduction expected for ULVZs. (d) Splitting intensities for the scenario shown in c, measured as in panel b.

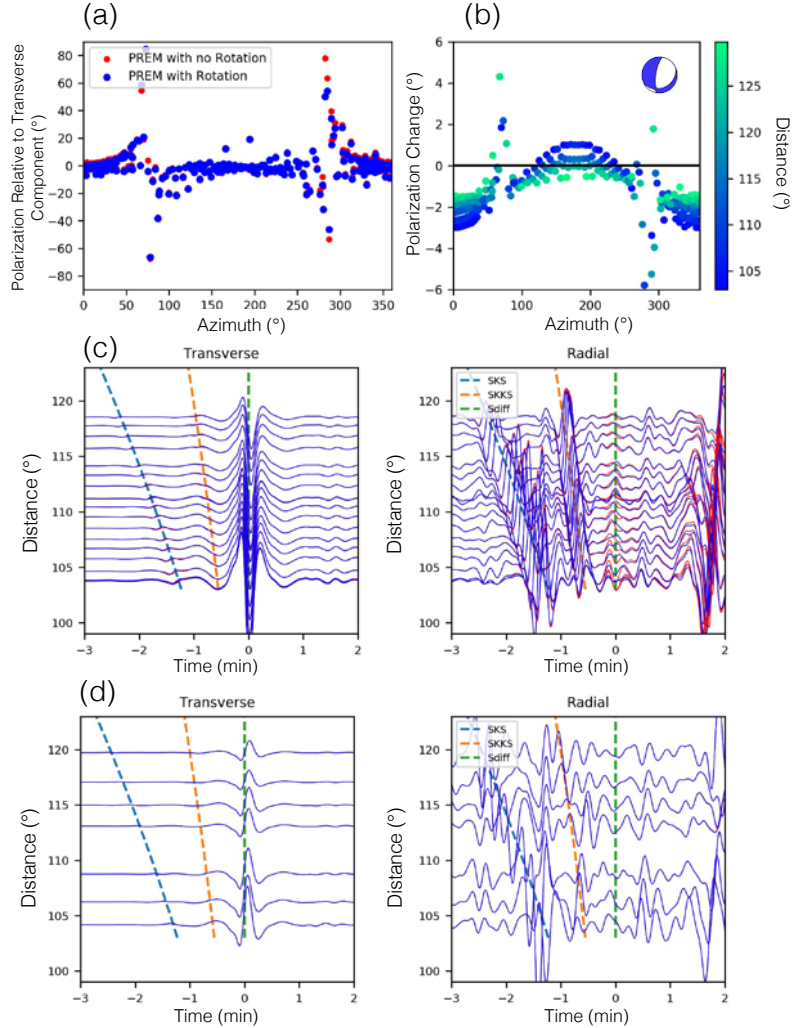


Figure 6: Results for simulations with and without Earth's rotation. (a) Angular deviations of  $S_{\text{diff}}$  polarization from the transverse component for a single, realistic event for isotropic PREM (depth = 616 km), where one simulation includes Earth's rotation (blue) and without (red) using SPECFEM3D.GLOBE. (b) The difference in angular deviations for a simulation including Earth's rotation and one without as determined from (a), where each point is colored by arc distance. The event's moment tensor is included at upper right. (c) A small selection of  $S_{\text{diff}}$  waveforms (for azimuths traversing north with an azimuth range of 340°-360°) from both simulations for the transverse (left) and radial (right) components (Note: radial waveforms are doubled relative to the transverse component to highlight the difference in waveform shape). Red waveforms represent simulations without Earth's rotation, while blue waveforms include rotation. Predicted PREM arrival times of SKS (light blue), SKKS (orange), and  $S_{\text{diff}}$  (green) are displayed as well. Waveforms are bandpass filtered (10 s-50 s). (d) Another selection of  $S_{\text{diff}}$  waveforms from the same event for azimuths 100°-130°, plotted with same conventions as (c).

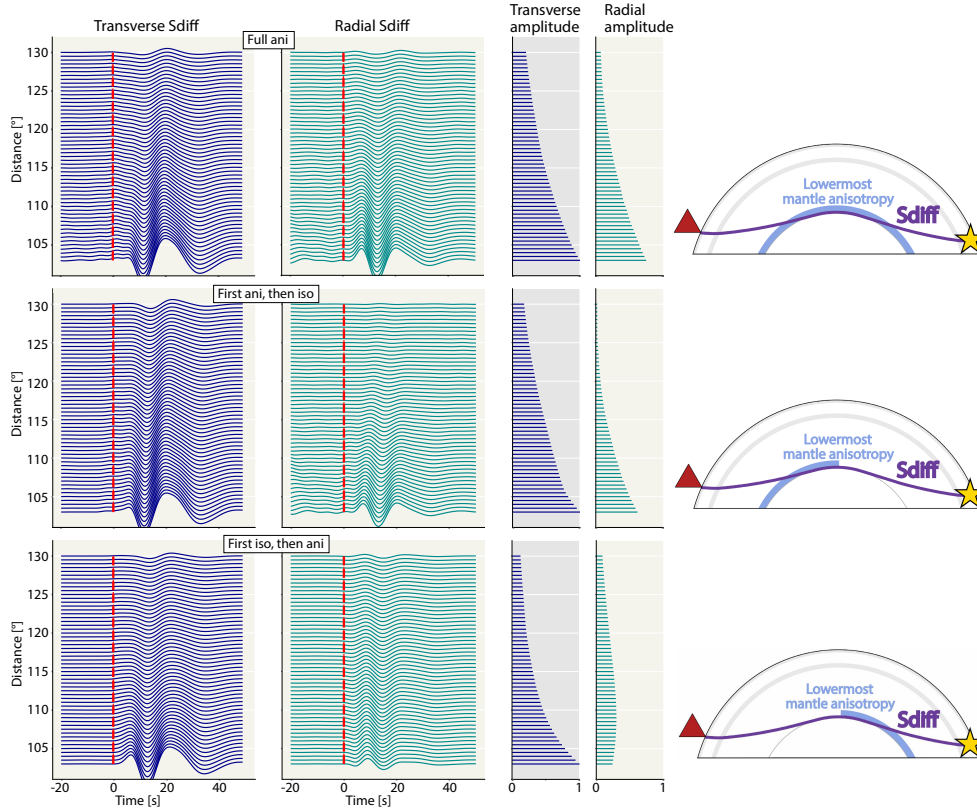


Figure 7: Results from synthetic calculations that use an isotropic PREM (Dziewonski and Anderson, 1981) input model, for which the bottom 150 km of the mantle were replaced by Ppv anisotropy, calculated for a focal depth of 500 km. The initial source polarization is SH for all simulations. (The reason for the difference in waveform shape compared to the previous figures is that we use a slightly different source-receiver configuration here, see Section 2.1). Transverse and radial  $S_{\text{diff}}$  waveforms (columns 1, 2) and corresponding amplitudes (columns 3, 4) are shown for three different cases. The amplitudes are plotted relative to the transverse  $S_{\text{diff}}$  amplitude at the lowest distance. These cases are schematically illustrated in the right column, showing raypaths (violet) from source (yellow star) to receiver (red triangle) for an epicentral distance of  $130^\circ$ , and the location of the lowermost mantle anisotropy (light blue). Upper row: full global layer of Ppv anisotropy (represented by light blue color in right column); middle row: lowermost mantle anisotropy, incorporated in the deep mantle up to an epicentral distance of  $65^\circ$  measured from the source (see right column); bottom row: lowermost mantle anisotropy from an epicentral distance of  $65^\circ$  from the source (see right column). Other plotting conventions are similar to Figure 3.

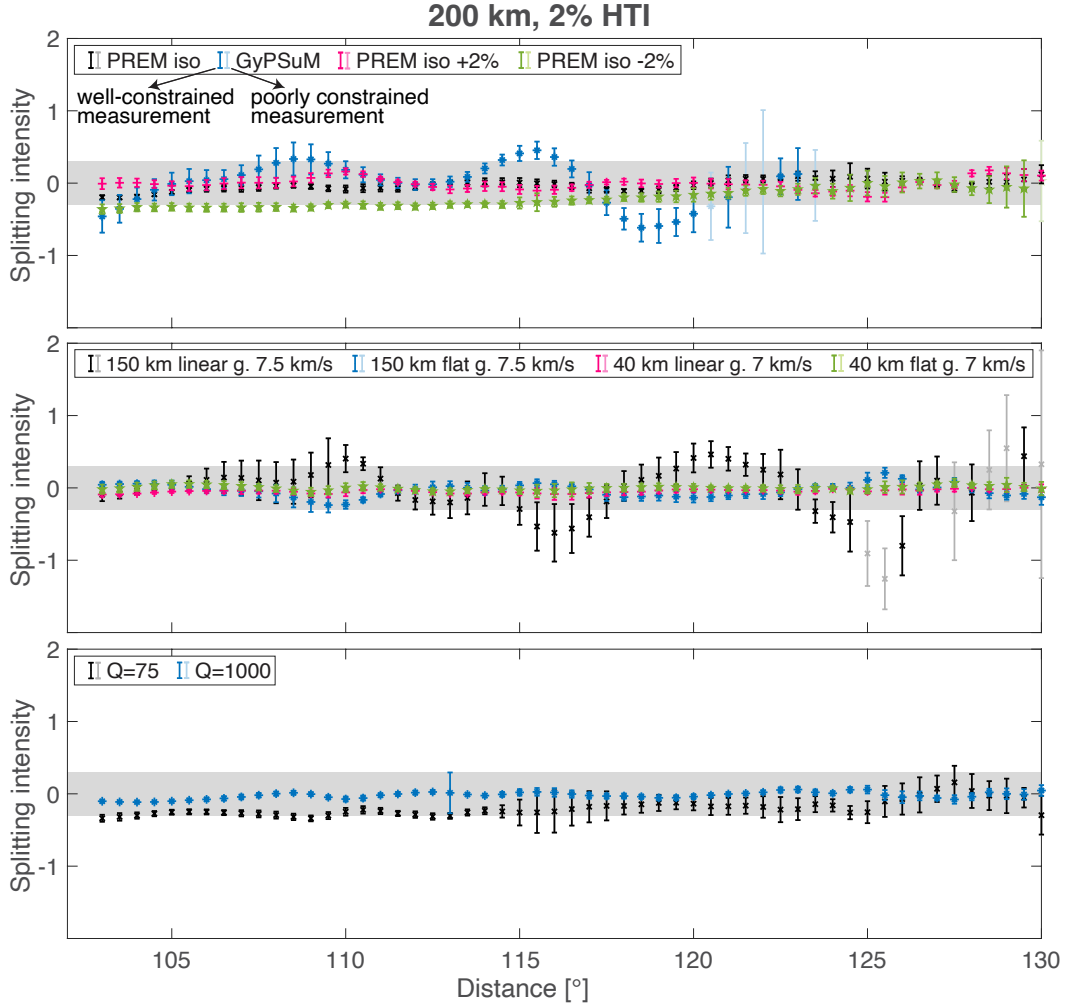


Figure 8: Results from simulations that incorporate only moderate source-side upper mantle anisotropy and no lowermost mantle anisotropy (200 km thick layer, 2% anisotropic strength for an HTI elastic tensor), plotted as  $SH_{\text{diff}}$  splitting intensities as a function of distance, calculated for a focal depth of 500 km.  $SI$  was measured using SplitRacer (Reiss and Rumpker, 2017). 95% confidence intervals are indicated by error bars. Simulations were conducted for all lowermost mantle properties tested in Section 3.1 (see legend). Simulations for which the lowermost mantle velocity was modified are shown in the top panel. These include an input model for which the mantle in PREM has been replaced by the GyPSuM tomographic model (Simmons et al., 2010; see legend). The middle panel shows results for different lowermost mantle velocity gradients, in particular, linear and flat gradients were tested (see legend). The bottom row presents results for two endmember Q-values. The shaded gray area indicates  $SI$ -values between  $-0.3$  and  $0.3$ , which would usually be defined as null. Results for simulations that include strong source-side anisotropy and are identical otherwise are shown in Supplementary Figure S5.

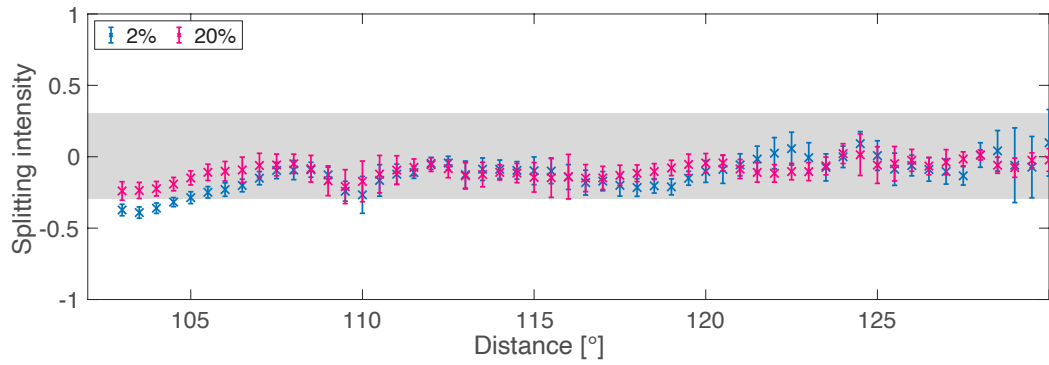


Figure 9: Simulation results, expressed as measured splitting intensities, for initially SH-polarized  $S_{\text{diff}}$  waves for two different velocity reductions at the base of the mantle, in presence of moderately strong source-side upper mantle anisotropy (200 km thick layer, 4% anisotropic strength for an HTI elastic tensor), calculated for a focal depth of 500 km. Plotting conventions are similar to Figure 8. Synthetics were computed for a 20 km thick low velocity layer at the base of the mantle. P wave velocity reductions are 1/3 of the S wave velocity reductions (see legend). 95% confidence intervals are shown by error bars. Almost all of the measurements are null (gray area). Results for other velocity reductions than those shown here are presented in Supplementary Figure S6.

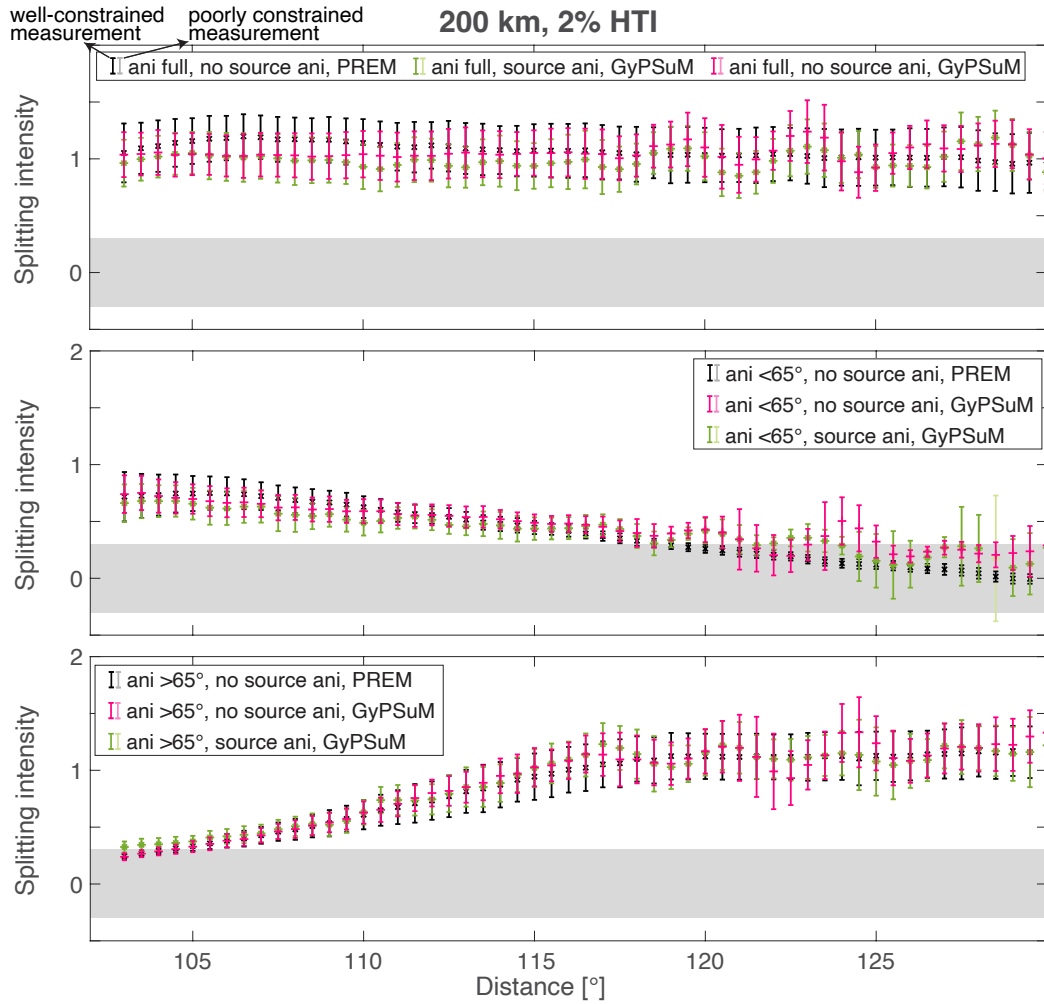


Figure 10: Results for similar scenarios of anisotropy in the lowermost mantle as shown in Figure 7, with similar plotting conventions as in Figure 8. Lowermost mantle anisotropy is incorporated for a full global layer of Ppv anisotropy, up to an epicentral distance of 65° (from the source) or from an epicentral distance of 65° (see legend). All simulations that use an isotropic PREM (Dziewonski and Anderson, 1981) without GyPSuM (Simmons et al., 2010) include lowermost mantle anisotropy only (see legend). Simulations with GyPSuM tomography in the mantle (replacing PREM velocity structure) include source and receiver side anisotropy (see legend). Results are shown for a moderately strongly anisotropic layer (as defined in the caption of Figure 8). Results for simulations that include strong source-side anisotropy and are otherwise identical are shown in Supplementary Figure S5.

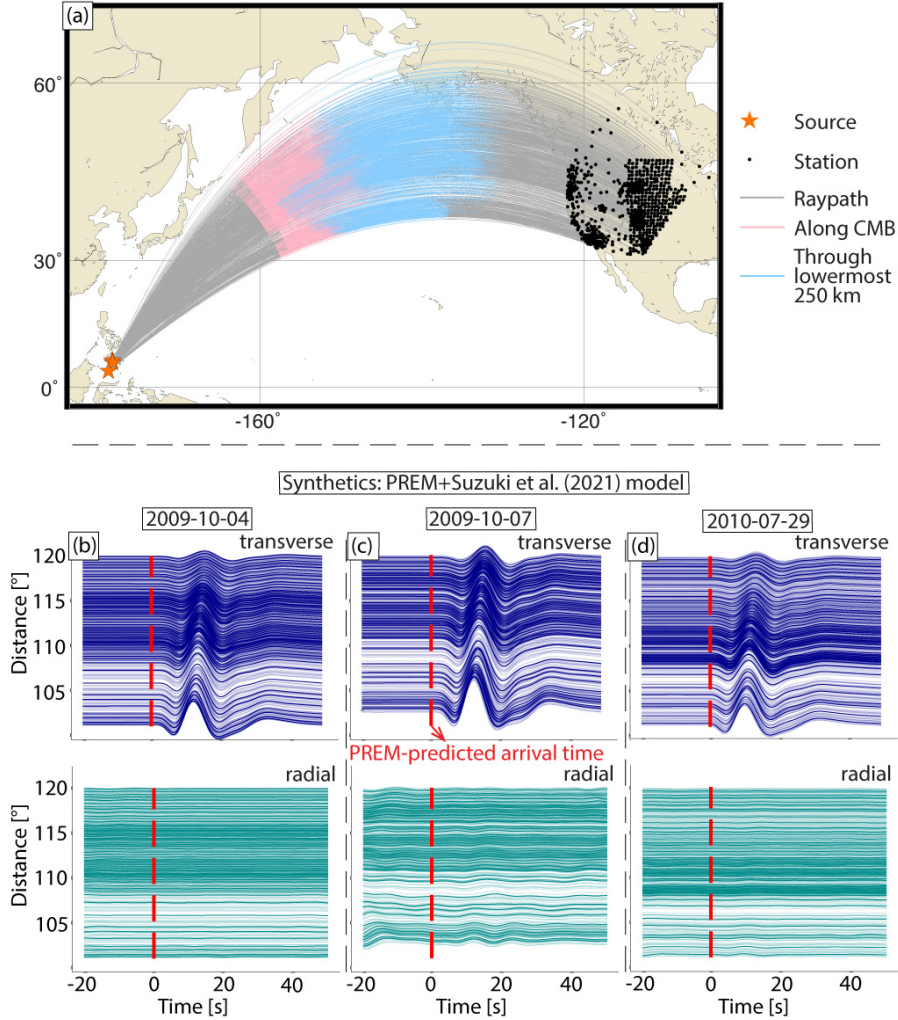


Figure 11: (a) Raypath and station distribution for the  $S_{\text{diff}}$  waves used in our real data example. Events are shown as orange stars, stations as black dots.  $S_{\text{diff}}$  raypaths for all three events are shown as solid gray lines. The path length along the CMB (pink) and through the lowermost mantle on the receiver side (blue) are emphasized. (b-d) Synthetic displacement seismograms calculated using an isotropic PREM (Dziewonski and Anderson, 1981) input model, for which lowermost mantle velocities have been replaced with an (isotropic) local 3-D velocity model for the lowermost mantle beneath the northern Pacific (Suzuki et al., 2021). Synthetic seismograms for events 2009-10-04 (b), 2009-10-07 (c) and 2010-07-29 (d) are shown as a function of epicentral distance. Seismograms are bandpass-filtered, retaining periods between 8 – 25 s. Transverse components (dark blue) are presented in the top row and radial components (teal) in the bottom row. Predicted  $S_{\text{diff}}$  arrival times according to PREM are indicated by red dashed lines. For all three events  $S_{\text{diff}}$  is almost fully SH polarized.

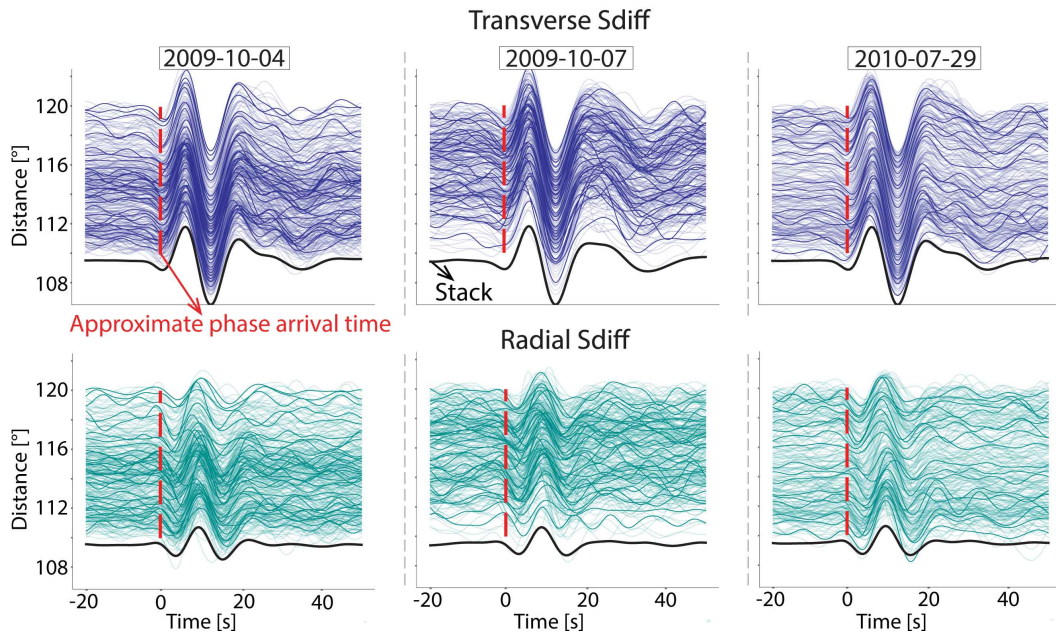


Figure 12: Transverse (top row) and radial (bottom row) component waveforms for the  $S_{\text{diff}}$  waves of all three events (left column: 2009-10-04; middle column: 2009-10-07; right column: 2010-07-29), recorded at a distance  $> 110^\circ$  and an azimuth  $< 43^\circ$  (see text). Waveforms are aligned and normalized with respect to the maximum radial  $S_{\text{diff}}$  amplitudes. Only every 10th trace is plotted without transparency to better visualize the individual waveforms. Red dashed lines represent approximate  $S_{\text{diff}}$  arrival times. Linearly stacked traces are plotted in black color on the corresponding panel.

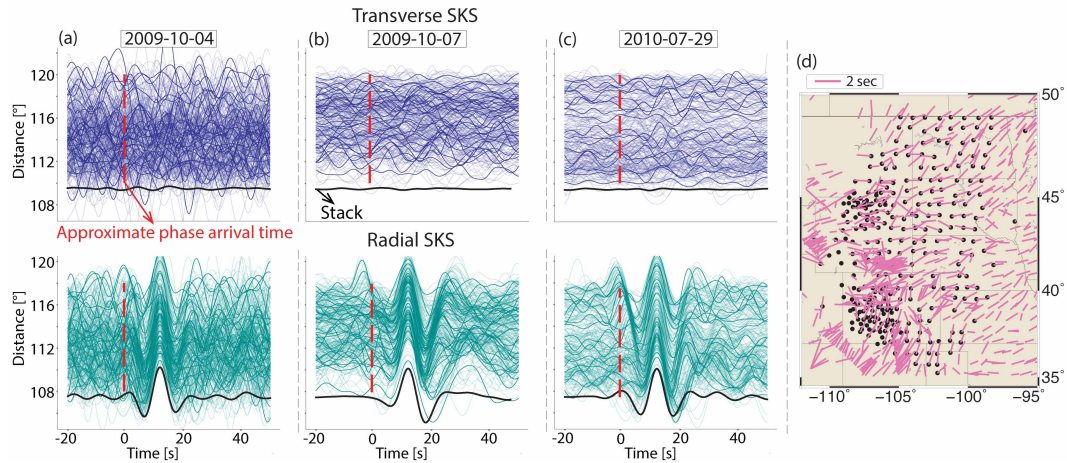


Figure 13: (a-c) SKS waveforms for the same selection of stations and events as in Figure 12. The same plotting conventions as in Figure 12 are used. (d) Zoom-in to the stations (black dots) used for event 2009-10-04. Splitting parameters from the IRIS splitting database (IRIS DMC, 2012) are shown as pink sticks. The orientation of the sticks indicates the fast polarization direction and their length is proportional to the delay time (see legend). Note that the station selection for the two other events is very similar but not identical (e.g., due to different timings of events).

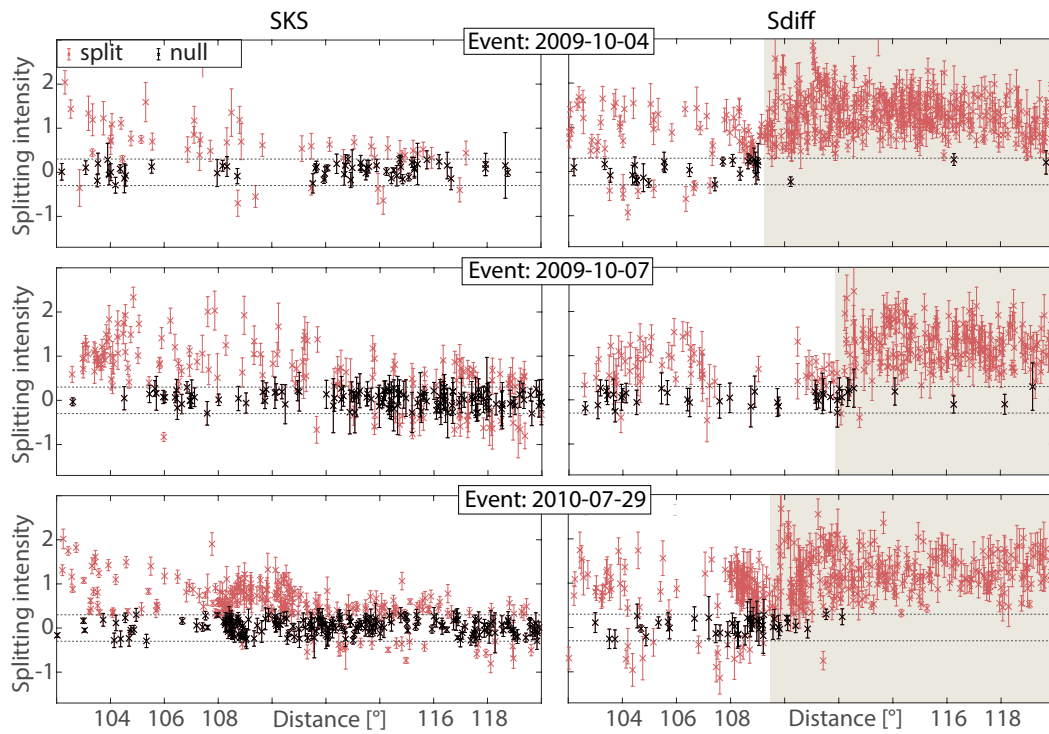


Figure 14: Measurement of splitting intensities for individual seismograms for three events, showing SKS (left column) and  $S_{\text{diff}}$  (right column). Top row: for event 2009-10-04; middle row: event 2009-10-07; bottom row: event 2010-07-29. Left column: SKS splitting intensities as a function of distance, measured using SplitRacer (Reiss and Rumpker, 2017). Null results (defined as  $|SI| < 0.3$ ) are plotted in black and split results in red. Error bars indicate 95% confidence intervals. Only high-quality measurements are retained (defined by a 95% confidence interval that is smaller than  $\pm 0.5$ ). Right column:  $S_{\text{diff}}$  splitting intensities as a function of distance using the same plotting conventions as for the left row. The area with tan shading indicates the distance range for which particularly strong  $S_{\text{diff}}$  splitting can be observed for each event.

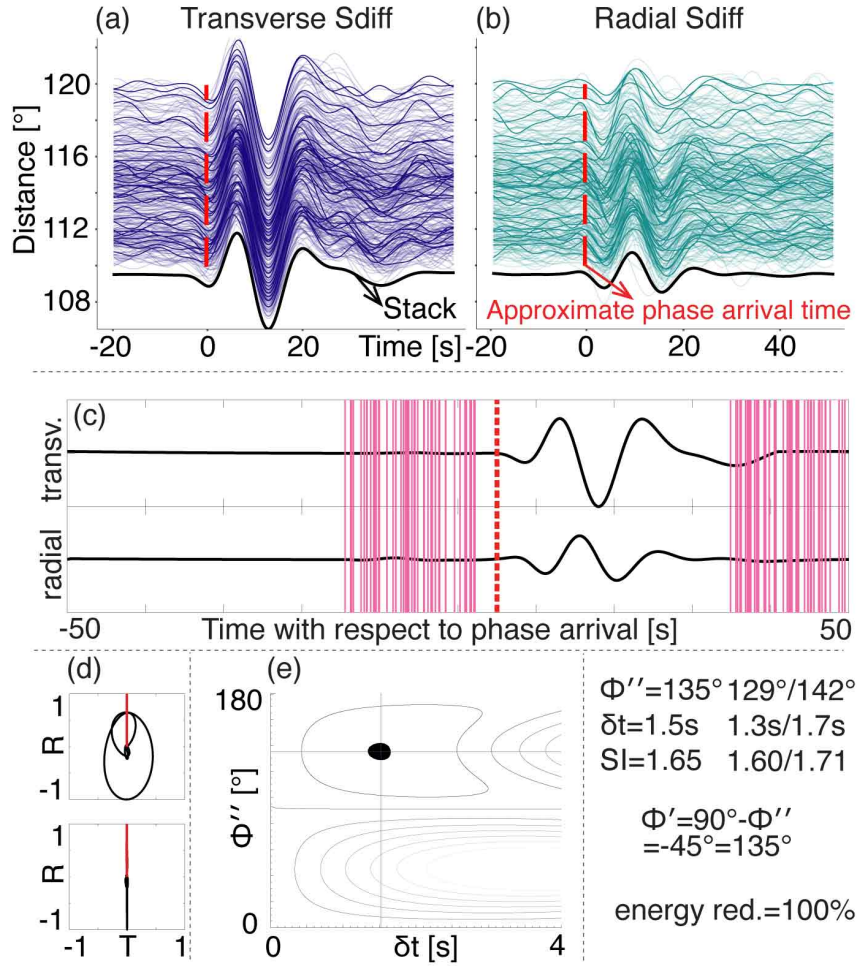


Figure 15:  $S_{\text{diff}}$  waveforms and splitting diagnostic plots from SplitRacer (Reiss and Rumpker, 2017) for event 2009-10-04. Similar plots for the other two events are shown in Supplementary Figures S11 and S12. In the waveform plots, approximate  $S_{\text{diff}}$  arrival times as are shown as a red dashed lines. (a) Transverse component waveforms recorded at a distance  $> 110^\circ$  and an azimuth  $< 43^\circ$  (see text). Waveforms were aligned and normalized with respect to the maximum transverse  $S_{\text{diff}}$  amplitudes. (b) Similar representation of the corresponding radial  $S_{\text{diff}}$  waveforms. Only every 10th trace is plotted without transparency to better visualize the individual waveforms. (c) Waveforms of the  $S_{\text{diff}}$  stack (radial, top trace; transverse, bottom trace) are shown as black solid lines and the start/end of the 50 randomly chosen measurement windows as pink lines. (d) The upper diagram shows the particle motion for the original stack, the lower diagrams for the waveforms that were corrected for splitting. The red lines in the diagrams indicate the backazimuthal direction. (e) The best fitting splitting parameters are shown in the  $\phi'' - \delta t$ -plane, with black color indicating the 95% confidence region. For an explanation of the splitting parameters  $\phi''$  and  $\phi'$  see Section 2.2.

908 **References**

- 909 Backus, G., Gilbert, F., 1961. The rotational splitting of the free oscillations of the earth.  
910 Proceedings of the National Academy of Sciences of the United States of America 47, 362.
- 911 Barruol, G., Kern, H., 1996. Seismic anisotropy and shear-wave splitting in lower-crustal  
912 and upper-mantle rocks from the Ivrea Zone: experimental and calculated data. Physics  
913 of the Earth and Planetary Interiors 95, 175–194. URL: [https://doi.org/10.1016/  
914 0031-9201\(95\)03124-3](https://doi.org/10.1016/0031-9201(95)03124-3).
- 915 Becker, T.W., Schaeffer, A.J., Lebedev, S., Conrad, C.P., 2015. Toward a generalized  
916 plate motion reference frame. Geophysical Research Letters 42, 3188 – 3196. URL:  
917 <https://doi.org/10.1002/2015GL063695>.
- 918 Beyreuther, M., Barsch, R., Krischer, L., Megies, T., Behr, Y., Wassermann, J., 2010.  
919 Obspy: A python toolbox for seismology. Seismological Research Letters 81, 530–533.  
920 URL: <https://doi.org/10.1111/10.1785/gssrl.81.3.530>.
- 921 Borgeaud, A.F., Konishi, K., Kawai, K., Geller, R.J., 2016. Finite frequency effects on  
922 apparent S-wave splitting in the D layer: comparison between ray theory and full-wave  
923 synthetics. Geophysical Journal International 207, 12–28. URL: [https://doi.org/10.  
924 1093/gji/ggw254](https://doi.org/10.1093/gji/ggw254).
- 925 Chang, S.J., Ferreira, A.M., Ritsema, J., van Heijst, H.J., Woodhouse, J.H., 2014. Global  
926 radially anisotropic mantle structure from multiple datasets: A review, current challenges,  
927 and outlook. Tectonophysics 617, 1–19. URL: [https://doi.org/10.1016/j.tecto.  
928 2014.01.033](https://doi.org/10.1016/j.tecto.2014.01.033).
- 929 Chang, S.J., Ferreira, A.M.G., 2019. Inference on Water Content in the Mantle Transition  
930 Zone Near Subducted Slabs From Anisotropy Tomography. Geochemistry, Geophysics,  
931 Geosystems 20, 1189–1201. URL: <https://doi.org/10.1029/2018GC008090>.
- 932 Chevrot, S., 2000. Multichannel analysis of shear wave splitting. Journal of Geophysical Re-  
933 search: Solid Earth 105, 21579–21590. URL: <https://doi.org/10.1029/2000JB900199>.
- 934 Cottaar, S., Romanowicz, B., 2013. Observations of changing anisotropy across the southern  
935 margin of the African LLSVP. Geophysical Journal International 195, 1184–1195. URL:  
936 <https://doi.org/10.1093/gji/ggt285>.
- 937 Creasy, N., Bozdog, E., Frost, D.A., Snieder, R., in review. Body Wave Polarization Anoma-  
938 lies due to Earth’s Coriolis Effect .

- 939 Creasy, N., Long, M.D., Ford, H.A., 2017. Deformation in the lowermost mantle beneath  
940 Australia from observations and models of seismic anisotropy. *Journal of Geophysical*  
941 *Research: Solid Earth* 122, 5243–5267. URL: <https://doi.org/10.1002/2016JB013901>.
- 942 Creasy, N., Miyagi, L., Long, M.D., 2020. A Library of Elastic Tensors for Lowermost  
943 Mantle Seismic Anisotropy Studies and Comparison With Seismic Observations. *Geo-*  
944 *chemistry, Geophysics, Geosystems* 21, e2019GC008883. URL: <https://doi.org/10.1029/2019GC008883>.
- 946 Creasy, N., Pisconti, A., Long, M.D., Thomas, C., 2021. Modeling of Seismic An-  
947 isotropy Observations Reveals Plausible Lowermost Mantle Flow Directions Beneath  
948 Siberia. *Geochemistry, Geophysics, Geosystems* 22, e2021GC009924. URL: <https://doi.org/10.1029/2021GC009924>.
- 950 Creasy, N., Pisconti, A., Long, M.D., Thomas, C., Wookey, J., 2019. Constraining lowermost  
951 mantle anisotropy with body waves: A synthetic modelling study. *Geophysical Journal*  
952 *International* 217, 766–783.
- 953 Crotwell, P., Owens, T.J., Ritsema, J., 1999. The TauP Toolkit: Flexible Seismic Travel-  
954 Time and Raypath Utilities. *Seismological Research Letters* 70. URL: <https://doi.org/10.1785/gssrl.70.2.154>.
- 956 Dahlen, F.A., Tromp, J., 1998. *Theoretical Global Seismology*. Princeton University Press.
- 957 Doornbos, D.J., Mondt, J.C., 1979. Attenuation of P and S waves diffracted around the  
958 core. *Geophysical Journal International* 57, 353–379. URL: <https://doi.org/10.1111/j.1365-246X.1979.tb04783.x>.
- 960 Dziewonski, A.M., Anderson, D.L., 1981. Preliminary reference Earth model. *Physics*  
961 *of the Earth and Planetary Interiors* 25, 297–356. URL: [https://doi.org/10.1016/0031-9201\(81\)90046-7](https://doi.org/10.1016/0031-9201(81)90046-7).
- 963 Ekström, G., Nettles, M., Dziewoński, A., 2012. The global cmt project 2004–2010:  
964 Centroid-moment tensors for 13,017 earthquakes. *Physics of the Earth and Planetary*  
965 *Interiors* 200, 1–9. URL: <https://doi.org/10.1016/j.pepi.2012.04.002>.
- 966 Erdman, M.E., Hacker, B.R., Zandt, G., Seward, G., 2013. Seismic anisotropy of the crust:  
967 electron-backscatter diffraction measurements from the Basin and Range. *Geophysical*  
968 *Journal International* 195, 1211–1229. URL: <https://doi.org/10.1093/gji/ggt287>.
- 969 Ferreira, A., Faccenda, M., Sturgeon, W., Chang, S.J., Schardong, L., 2019. Ubiquitous  
970 lower-mantle anisotropy beneath subduction zones. *Nature Geoscience* 12, 301—306.  
971 URL: <https://doi.org/10.1038/s41561-019-0325-7>.

- 972 Foley, B.J., Long, M.D., 2011. Upper and mid-mantle anisotropy beneath the Tonga slab.  
973 Geophysical Research Letters 38. URL: <https://doi.org/10.1029/2010GL046021>.
- 974 Ford, H.A., Long, M.D., He, X., Lynner, C., 2015. Lowermost mantle flow at the eastern  
975 edge of the African Large Low Shear Velocity Province. Earth and Planetary Science  
976 Letters 420, 12–22. URL: <https://doi.org/10.1016/j.epsl.2015.03.029>.
- 977 Fouch, M.J., Fischer, K.M., Wyssession, M.E., 2001. Lowermost mantle anisotropy beneath  
978 the Pacific: Imaging the source of the Hawaiian plume. Earth and Planetary Science  
979 Letters 190, 167–180. URL: [https://doi.org/10.1016/S0012-821X\(01\)00380-6](https://doi.org/10.1016/S0012-821X(01)00380-6).
- 980 French, S.W., Romanowicz, B.A., 2014. Whole-mantle radially anisotropic shear velocity  
981 structure from spectral-element waveform tomography. Geophysical Journal International  
982 199, 1303–1327. URL: <https://doi.org/10.1093/gji/ggu334>.
- 983 Frost, D.A., Lasbleis, M., Chandler, B., Romanowicz, B., 2021. Dynamic history of the  
984 inner core constrained by seismic anisotropy. Nature Geoscience , 531–535 URL: <https://doi.org/10.1038/s41561-021-00761-w>.
- 986 Garnero, E.J., Lay, T., 1997. Lateral variations in lowermost mantle shear wave anisotropy  
987 beneath the north Pacific and Alaska. Journal of Geophysical Research: Solid Earth 102,  
988 8121–8135. URL: <https://doi.org/10.1029/96JB03830>.
- 989 Garnero, E.J., Moore, M.M., Lay, T., Fouch, M.J., 2004. Isotropy or weak vertical transverse  
990 isotropy in D” beneath the Atlantic Ocean. Journal of Geophysical Research: Solid Earth  
991 109, 1–10. URL: <https://doi.org/10.1029/2004JB003004>.
- 992 IRIS DMC, 2012. Data Services Products: SWS-DBs Shear-wave splitting databases. URL:  
993 <https://doi.org/10.17611/DP/SWS.1>.
- 994 IRIS Transportable Array, 2003. USArray Transportable Array. URL: <https://www.fdsn.org/networks/detail/TA/>, doi:10.7914/SN/TA.
- 996 Karato, S.I., Jung, H., Katayama, I., Skemer, P., 2008. Geodynamic Significance of Seismic  
997 Anisotropy of the Upper Mantle: New Insights from Laboratory Studies. Annual Review  
998 of Earth and Planetary Sciences 36, 59–95. URL: <https://doi.org/10.1146/annurev.earth.36.031207.124120>.
- 1000 Komatitsch, D., Tromp, J., 2002a. Spectral-element simulations of global seismic wave  
1001 propagation—I. Validation. Geophysical Journal International 149, 390–412. URL:  
1002 <https://doi.org/10.1046/j.1365-246X.2002.01653.x>.

- 1003 Komatitsch, D., Tromp, J., 2002b. Spectral-element simulations of global seismic wave prop-  
1004 agation—II. Three-dimensional models, oceans, rotation and self-gravitation. *Geophysi-*  
1005 *cal Journal International* 150, 303–318. URL: [https://doi.org/10.1046/j.1365-246X.](https://doi.org/10.1046/j.1365-246X.2002.01716.x)  
1006 [2002.01716.x](https://doi.org/10.1046/j.1365-246X.2002.01716.x).
- 1007 Komatitsch, D., Vinnik, L.P., Chevrot, S., 2010. SHdiff-SVdiff splitting in an isotropic  
1008 Earth. *Journal of Geophysical Research: Solid Earth* 115. URL: [https://doi.org/10.](https://doi.org/10.1029/2009JB006795)  
1009 [1029/2009JB006795](https://doi.org/10.1029/2009JB006795).
- 1010 Lawrence, J.F., Wysession, M.E., 2006. QLM9: A new radial quality factor (Q) model  
1011 for the lower mantle. *Earth and Planetary Science Letters* 241, 962–971. URL: [https:](https://doi.org/10.1016/j.epsl.2005.10.030)  
1012 [//doi.org/10.1016/j.epsl.2005.10.030](https://doi.org/10.1016/j.epsl.2005.10.030).
- 1013 Lay, T., Williams, Q., Garnero, E.J., Kellogg, L., Wysession, M.E., 1998. Seismic Wave  
1014 Anisotropy in the D Region and Its Implications. American Geophysical Union (AGU).  
1015 pp. 299–318. URL: <https://doi.org/10.1029/GD028p0299>.
- 1016 Leng, K., Nissen-Meyer, T., van Driel, M., 2016. Efficient global wave propagation adapted  
1017 to 3-D structural complexity: a pseudospectral/spectral-element approach. *Geophysical*  
1018 *Journal International* 207, 1700–1721. URL: <https://doi.org/10.1093/gji/ggw363>.
- 1019 Leng, K., Nissen-Meyer, T., van Driel, M., Hosseini, K., Al-Attar, D., 2019. AxiSEM3D:  
1020 broad-band seismic wavefields in 3-D global earth models with undulating discontinuities.  
1021 *Geophysical Journal International* 217, 2125–2146. URL: [https://doi.org/10.1093/](https://doi.org/10.1093/gji/ggz092)  
1022 [gji/ggz092](https://doi.org/10.1093/gji/ggz092).
- 1023 Long, M.D., Becker, T., 2010. Mantle dynamics and seismic anisotropy. *Earth and Planetary*  
1024 *Science Letters* 297, 341–354. URL: <https://doi.org/10.1016/j.epsl.2010.06.036>.
- 1025 Long, M.D., Silver, P.G., 2009. Shear Wave Splitting and Mantle Anisotropy: Measure-  
1026 ments, Interpretations, and New Directions. *Surveys in Geophysics* 30, 407–461. URL:  
1027 <https://doi.org/10.1007/s10712-009-9075-1>.
- 1028 Lutz, K., Long, M., Creasy, N., Deng, J., 2020. Seismic anisotropy in the lowermost mantle  
1029 beneath North America from SKS-SKKS splitting intensity discrepancies. *Physics of the*  
1030 *Earth and Planetary Interiors* 305, 106504. URL: [https://doi.org/10.1016/j.pepi.](https://doi.org/10.1016/j.pepi.2020.106504)  
1031 [2020.106504](https://doi.org/10.1016/j.pepi.2020.106504).
- 1032 Lynner, C., Long, M.D., 2014. Lowermost mantle anisotropy and deformation along the  
1033 boundary of the African LLSVP. *Geophysical Research Letters* , 3447–3454 URL: [https:](https://doi.org/10.1002/2014GL059875)  
1034 [//doi.org/10.1002/2014GL059875](https://doi.org/10.1002/2014GL059875).

- 1035 Lynner, C., Long, M.D., 2015. Heterogeneous seismic anisotropy in the transition zone and  
1036 uppermost lower mantle: evidence from South America, Izu-Bonin and Japan. *Geophysical*  
1037 *Journal International* 201, 1545–1552. URL: <https://doi.org/10.1093/gji/ggv099>.
- 1038 Masters, G., Park, J., Gilbert, F., 1983. Observations of coupled spheroidal and toroidal  
1039 modes. *Journal of Geophysical Research: Solid Earth* 88, 10285–10298. URL: <https://doi.org/10.1029/JB088iB12p10285>.
- 1041 Mohiuddin, A., D. Long, M., Lynner, C., 2015. Mid-mantle seismic anisotropy beneath  
1042 Southwestern Pacific subduction systems and implications for mid-mantle deformation.  
1043 *Physics of the Earth and Planetary Interiors* 245. URL: [https://doi.org/10.1016/j.](https://doi.org/10.1016/j.pepi.2015.05.003)  
1044 [pepi.2015.05.003](https://doi.org/10.1016/j.pepi.2015.05.003).
- 1045 Nowacki, A., Wookey, J., 2016. The limits of ray theory when measuring shear wave splitting  
1046 in the lowermost mantle with ScS waves. *Geophysical Journal International* 207, 1573–  
1047 1583. URL: <https://doi.org/10.1093/gji/ggw358>.
- 1048 Nowacki, A., Wookey, J., Kendall, J.M., 2010. Deformation of the lowermost mantle  
1049 from seismic anisotropy. *Nature* 467, 1091–1094. URL: [https://doi.org/10.1038/](https://doi.org/10.1038/nature09507)  
1050 [nature09507](https://doi.org/10.1038/nature09507).
- 1051 Nowacki, A., Wookey, J., Kendall, J.M., 2011. New advances in using seismic anisotropy,  
1052 mineral physics and geodynamics to understand deformation in the lowermost mantle.  
1053 *Journal of Geodynamics* 52, 205–228. URL: [https://doi.org/10.1016/j.jog.2011.](https://doi.org/10.1016/j.jog.2011.04.003)  
1054 [04.003](https://doi.org/10.1016/j.jog.2011.04.003).
- 1055 Panning, M., Romanowicz, B., 2006. A three-dimensional radially anisotropic model of  
1056 shear velocity in the whole mantle. *Geophysical Journal International* 167, 361–379.  
1057 URL: <https://doi.org/10.1111/j.1365-246X.2006.03100.x>.
- 1058 Parisi, L., Ferreira, A.M.G., Ritsema, J., 2018. Apparent Splitting of S Waves Propagating  
1059 Through an Isotropic Lowermost Mantle. *Journal of Geophysical Research: Solid Earth*  
1060 123, 3909–3922. URL: <https://doi.org/10.1002/2017JB014394>.
- 1061 Park, J., Gilbert, F., 1986. Coupled free oscillations of an aspherical, dissipative, rotating  
1062 earth: Galerkin theory. *Journal of Geophysical Research: Solid Earth* 91, 7241–7260.
- 1063 Reiss, M., Rumpker, G., 2017. SplitRacer: MATLAB Code and GUI for Semiautomated  
1064 Analysis and Interpretation of Teleseismic Shear-Wave Splitting. *Seismological Research*  
1065 *Letters* 88, 392 — 409. URL: <https://doi.org/10.1785/0220160191>.

- 1066 Reiss, M.C., Long, M.D., Creasy, N., 2019. Lowermost Mantle Anisotropy Beneath Africa  
1067 From Differential SKS-SKKS Shear-Wave Splitting. *Journal of Geophysical Research:*  
1068 *Solid Earth* 124, 8540–8564. URL: <https://doi.org/10.1029/2018JB017160>.
- 1069 Ritsema, J., Deuss, A., van Heijst, H.J., Woodhouse, J.H., 2011. S40RTS: a degree-40 shear-  
1070 velocity model for the mantle from new Rayleigh wave dispersion, teleseismic traveltimes  
1071 and normal-mode splitting function measurements. *Geophysical Journal International*  
1072 184, 1223–1236. URL: <https://doi.org/10.1111/j.1365-246X.2010.04884.x>.
- 1073 Ritsema, J., Lay, T., Garnero, E., Benz, H., 1998. Seismic anisotropy in the lowermost  
1074 mantle beneath the Pacific. *Geophysical Research Letters* 25, 1229–1232. URL: <https://doi.org/10.1029/98GL00913>.
- 1076 Romanowicz, B., Cao, A., Godwal, B., Wenk, R., Ventosa, S., Jeanloz, R., 2016. Seismic  
1077 anisotropy in the Earth's innermost inner core: Testing structural models against mineral  
1078 physics predictions. *Geophysical Research Letters* 43, 93 – 100. URL: <https://doi.org/10.1002/2015GL066734>.
- 1080 Romanowicz, B., Mitchell, B., 2007. Deep Earth Structure -Q of the Earth from  
1081 Crust to Core. *Treatise on Geophysics*, 731–774 URL: [https://doi.org/10.1016/](https://doi.org/10.1016/B978-044452748-6.00024-9)  
1082 [B978-044452748-6.00024-9](https://doi.org/10.1016/B978-044452748-6.00024-9).
- 1083 Russo, R., Gallego, A., Comte, D., Mocanu, V., Murdie, R., VanDecar, J., 2010. Source-  
1084 side shear wave splitting and upper mantle flow in the Chile Ridge subduction Region.  
1085 *Geology* 38, 707–710. URL: <https://doi.org/10.1130/G30920.1>.
- 1086 Schoenberg, M., Censor, D., 1973. Elastic waves in rotating media. *Quarterly of Applied*  
1087 *Mathematics* 31, 115–125.
- 1088 Silver, P.G., 1996. Seismic Anisotropy beneath the Continents: Probing the Depths of  
1089 Geology. *Annual Review of Earth and Planetary Sciences* 24, 385 – 432. URL: <https://doi.org/10.1146/annurev.earth.24.1.385>.
- 1091 Silver, P.G., Chan, W.W., 1991. Shear wave splitting and subcontinental mantle de-  
1092 formation. *Journal of Geophysical Research: Solid Earth* 96, 16429–16454. URL:  
1093 <https://doi.org/10.1029/91JB00899>.
- 1094 Simmons, N.A., Forte, A.M., Boschi, L., Grand, S.P., 2010. GyPSuM: A joint tomographic  
1095 model of mantle density and seismic wave speeds. *Journal of Geophysical Research: Solid*  
1096 *Earth* 115. URL: <https://doi.org/10.1029/2010JB007631>.
- 1097 Snieder, R., Sens-Schönfelder, C., 2021. Local coupling and conversion of surface waves due  
1098 to Earth's rotation. part 1: theory. *Geophysical Journal International* 225, 158–175.

- 1099 Snieder, R., Sens-Schönfelder, C., Ruigrok, E., Shiomi, K., 2016. Seismic shear waves as  
1100    foucault pendulum. *Geophysical Research Letters* 43, 2576–2581.
- 1101 Stackhouse, S., Brodholt, J.P., Wookey, J., Kendall, J.M., Price, G.D., 2005. The effect of  
1102    temperature on the seismic anisotropy of the perovskite and post-perovskite polymorphs  
1103    of MgSiO<sub>3</sub>. *Earth and Planetary Science Letters* 230, 1–10.
- 1104 Suzuki, Y., Kawai, K., Geller, R., 2021. Imaging paleoslabs and inferring the Clapeyron  
1105    slope in D" beneath the northern Pacific based on high-resolution inversion of seismic  
1106    waveforms for 3-D transversely isotropic structure. *Physics of the Earth and Planetary  
1107    Interiors* 321, 106751. URL: <https://doi.org/10.1016/j.pepi.2021.106751>.
- 1108 Tesoniero, A., Leng, K., D'Long, M., Nissen-Meyer, T., 2020. Full wave sensitivity of  
1109    SK(K)S phases to arbitrary anisotropy in the upper and lower mantle. *Geophysical Jour-  
1110    nal International* 222, 412 – 435. URL: <https://doi.org/10.1093/gji/ggaa171>.
- 1111 Towns, J., Cockerill, T., Dahan, M., Foster, I., Gaither, K., Grimshaw, A., Hazlewood,  
1112    V., Lathrop, S., Lifka, D., Peterson, G.D., et al., 2014. Xsede: accelerating scientific  
1113    discovery. *Computing in science & engineering* 16, 62–74.
- 1114 Tromp, J., 1994. Surface-wave propagation on a rotating, anisotropic earth. *Geophysical  
1115    Journal International* 117, 141–152.
- 1116 Vinnik, L., Breger, L., Romanowicz, B., 1998a. Anisotropic structures at the base of the  
1117    Earth's mantle. *Nature* 393, 564–567. doi:10.1038/31208.
- 1118 Vinnik, L., Bréger, L., Romanowicz, B., 1998b. On the inversion of Sd particle motion  
1119    for seismic anisotropy in D'. *Geophysical Research Letters* 25, 679–682. URL: <https://doi.org/10.1029/98GL00190>.
- 1120    //doi.org/10.1029/98GL00190.
- 1121 Vinnik, L., Farra, V., Romanowicz, B., 1989. Observational evidence for diffracted SV in  
1122    the shadow of the Earth's core. *Geophysical Research Letters - GEOPHYS RES LETT*  
1123    16, 519–522. URL: <https://doi.org/10.1029/98GL016i006p00519>.
- 1124 Vinnik, L., Romanowicz, B., Le Stunff, Y., Makeyeva, L., 1995. Seismic anisotropy in the D"  
1125    layer. *Geophysical Research Letters* 22, 1657–1660. URL: [https://doi.org/10.1029/  
1126    95GL01327](https://doi.org/10.1029/95GL01327).
- 1127 Walker, A., Wookey, J., 2012. MSAT - a new toolkit for the analysis of elastic and seismic  
1128    anisotropy. *Computers and Geosciences* 49, 81–90. URL: [https://doi.org/10.1016/j.  
1129    cageo.2012.05.031](https://doi.org/10.1016/j.cageo.2012.05.031).

- 1130 Walsh, E., Arnold, R., Savage, M.K., 2013. Silver and Chan revisited. *Journal of Geophysical*  
1131 *Research: Solid Earth* 118, 5500–5515. URL: <https://doi.org/10.1002/jgrb.50386>.
- 1132 Wessel, P., Smith, W.H.F., 1998. New, improved version of generic mapping tools released.  
1133 *Eos, Transactions American Geophysical Union* 79, 579–579. URL: [https://doi.org/](https://doi.org/10.1029/98E000426)  
1134 [10.1029/98E000426](https://doi.org/10.1029/98E000426).
- 1135 Wolf, J., Creasy, N., Pisconti, A., Long, M.D., Thomas, C., 2019. An investigation of seismic  
1136 anisotropy in the lowermost mantle beneath Iceland. *Geophysical Journal International*  
1137 219, S152 – S166. URL: <https://doi.org/10.1093/gji/ggz312>.
- 1138 Wolf, J., Long, M.D., 2022. Slab-driven flow at the base of the mantle beneath the  
1139 northeastern pacific ocean. *Earth and Planetary Science Letters* 594, 117758. URL:  
1140 <https://doi.org/10.1016/j.epsl.2022.117758>.
- 1141 Wolf, J., Long, M.D., Leng, K., Nissen-Meyer, T., 2022a. Constraining deep mantle aniso-  
1142 tropy with shear wave splitting measurements: Challenges and new measurement strate-  
1143 gies. *Geophysical Journal International* , 507–527URL: [https://doi.org/10.1093/gji/](https://doi.org/10.1093/gji/ggac055)  
1144 [ggac055](https://doi.org/10.1093/gji/ggac055).
- 1145 Wolf, J., Long, M.D., Leng, K., Nissen-Meyer, T., 2022b. Sensitivity of SK(K)S and ScS  
1146 phases to heterogeneous anisotropy in the lowermost mantle from global wavefield sim-  
1147 ulations. *Geophysical Journal International* 228, 366–386. URL: [https://doi.org/10.](https://doi.org/10.1093/gji/ggab347)  
1148 [1093/gji/ggab347](https://doi.org/10.1093/gji/ggab347).
- 1149 Wookey, J., Kendall, J.M., Rumpker, G., 2005. Lowermost mantle anisotropy beneath the  
1150 north Pacific from differential S-ScS splitting. *Geophysical Journal International* 161,  
1151 829–838. URL: <https://doi.org/10.1111/j.1365-246X.2005.02623.x>.
- 1152 Yu, S., Garnero, E.J., 2018. Ultralow Velocity Zone Locations: A Global Assessment. *Geo-*  
1153 *chemistry, Geophysics, Geosystems* URL: <https://doi.org/10.1002/2017GC007281>.
- 1154 Yuan, K., Beghein, C., 2014. Three-dimensional variations in Love and Rayleigh wave  
1155 azimuthal anisotropy for the upper 800km of the mantle. *Journal of Geophysical Research:*  
1156 *Solid Earth* 119, 3232–3255. URL: <https://doi.org/10.1002/2013JB010853>.

1 Supplementary Information – On the measurement of  $S_{\text{diff}}$  splitting caused by  
 2 lowermost mantle anisotropy

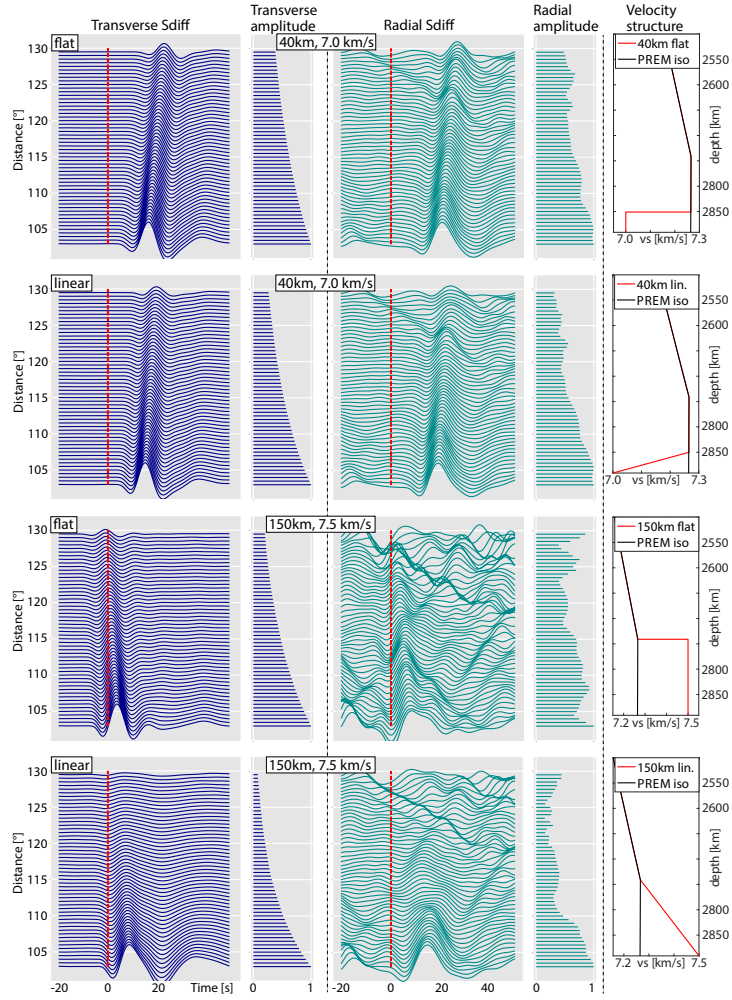


Figure S1: Representation of the transverse (left column, dark blue) and radial (third column, teal)  $S_{\text{diff}}$  waveforms as a function of epicentral distance. Transverse (second column, dark blue) and radial (fourth column, teal) amplitudes are also shown.  $S_{\text{diff}}$  arrival times predicted by PREM are represented as red dashed lines. Waveforms are shown for four cases that all use isotropic PREM as their background model. Top row: 40 km thick layer at the base of the mantle with shear wave speeds of  $7.0 \frac{\text{km}}{\text{s}}$  (right column); second row: velocity of  $7.0 \frac{\text{km}}{\text{s}}$  at the base of the mantle and a linear gradient to PREM-like velocities 40 km above the CMB (right column); third row: 150 km thick layer at the base of the mantle with shear wave speeds of  $7.5 \frac{\text{km}}{\text{s}}$  (see right column); bottom row: and a velocity of  $7.5 \frac{\text{km}}{\text{s}}$  at the base of the mantle and a linear gradient to PREM-like velocities 150 km above the CMB (see right column).

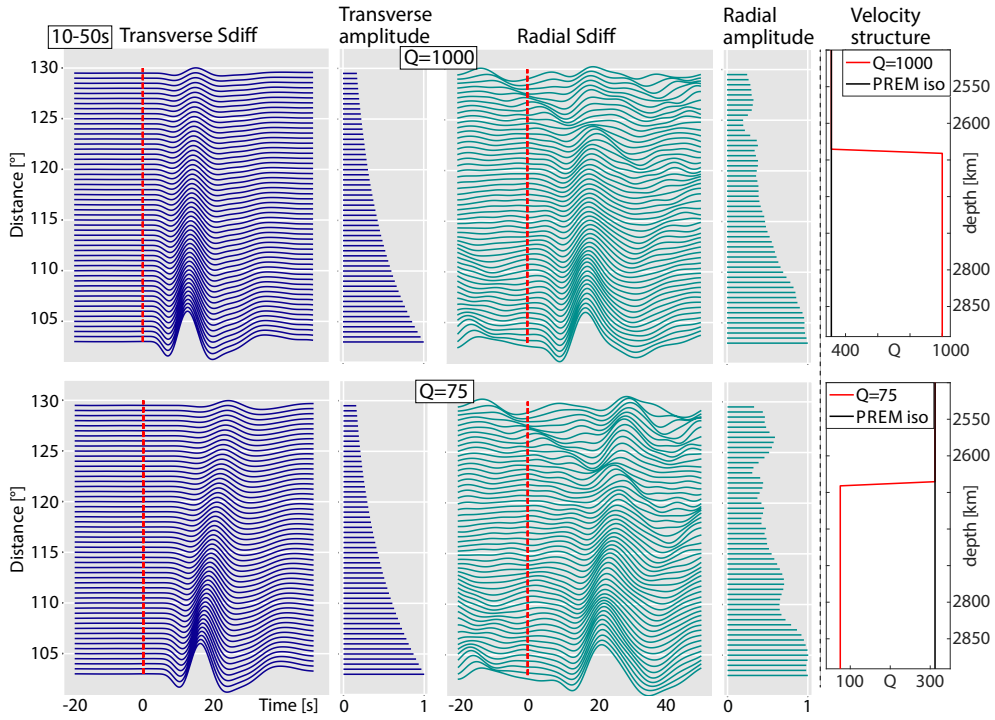


Figure S2: Transverse and radial  $S_{\text{diff}}$  waveforms and amplitudes for shear quality factor values  $Q_{\mu}$  (throughout this work called  $Q$ ) of 1000 (upper and third row) and 75 (second and bottom row) in the lowermost mantle. Waveforms were bandpass-filtered, retaining frequencies between 10 – 50 s. Plotting conventions are the same as in Figure S1.

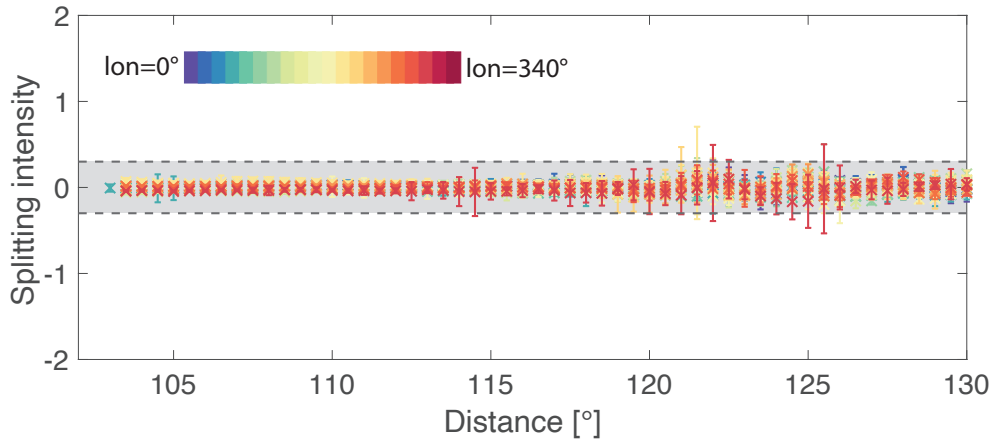


Figure S3: Splitting intensities as a function of distance for analogue source-receiver configurations along different longitudes (with a spacing of  $20^{\circ}$ ; see legend). All splitting intensity measurements are null ( $|SI| < 0.3$ ; indicated by black dashed lines). This figure is similar to Figure 5b of the main manuscript. The only difference is that S40RTS was used instead of GyPSuM.

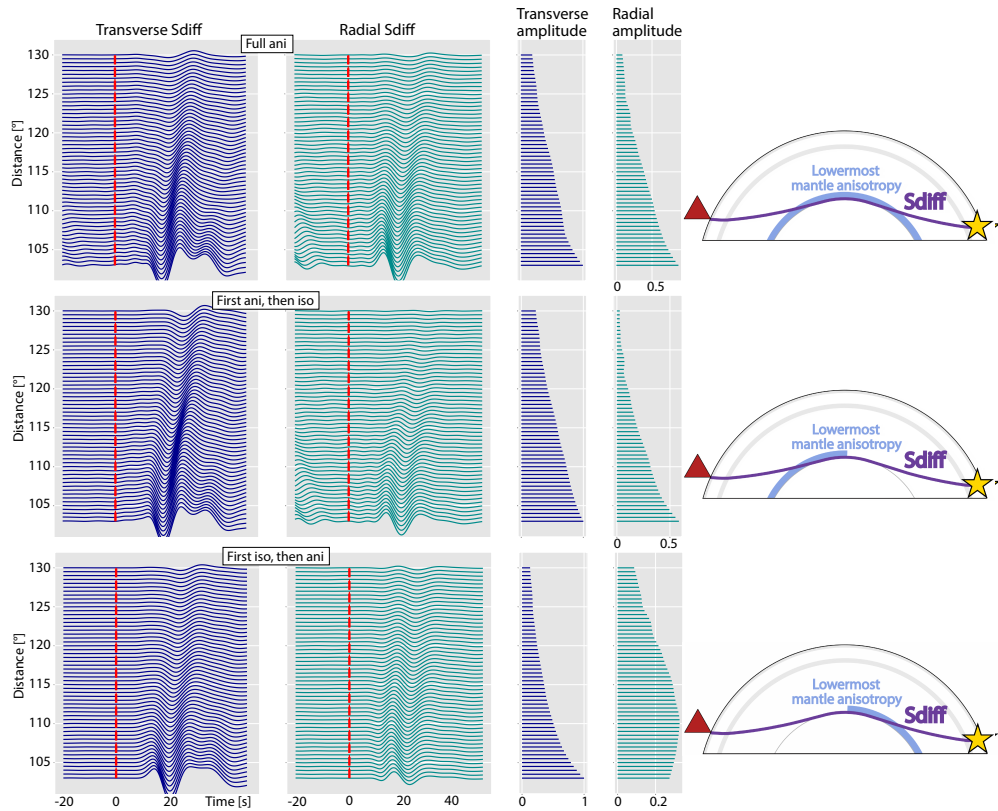


Figure S4: Similar to Figure 6 of the main manuscript using the GyPSuM tomography model for the mantle. Transverse and radial  $S_{diff}$  waveforms (columns 1, 2) and corresponding amplitudes (columns 3, 4) are shown for three different scenarios. These different scenarios are schematically illustrated in the right column, that shows raypaths (violet) from source (yellow star) to receiver (red triangle), and the location of the lowermost mantle anisotropy (light blue). Upper row: for a full global layer of Ppv anisotropy (represented by light blue color in right column); middle row: Lowermost mantle anisotropy, incorporated in the deep mantle up to an epicentral distance of  $65^\circ$  measured from the source (see right column); bottom row: from an epicentral distance of  $65^\circ$  from the source (see right column).

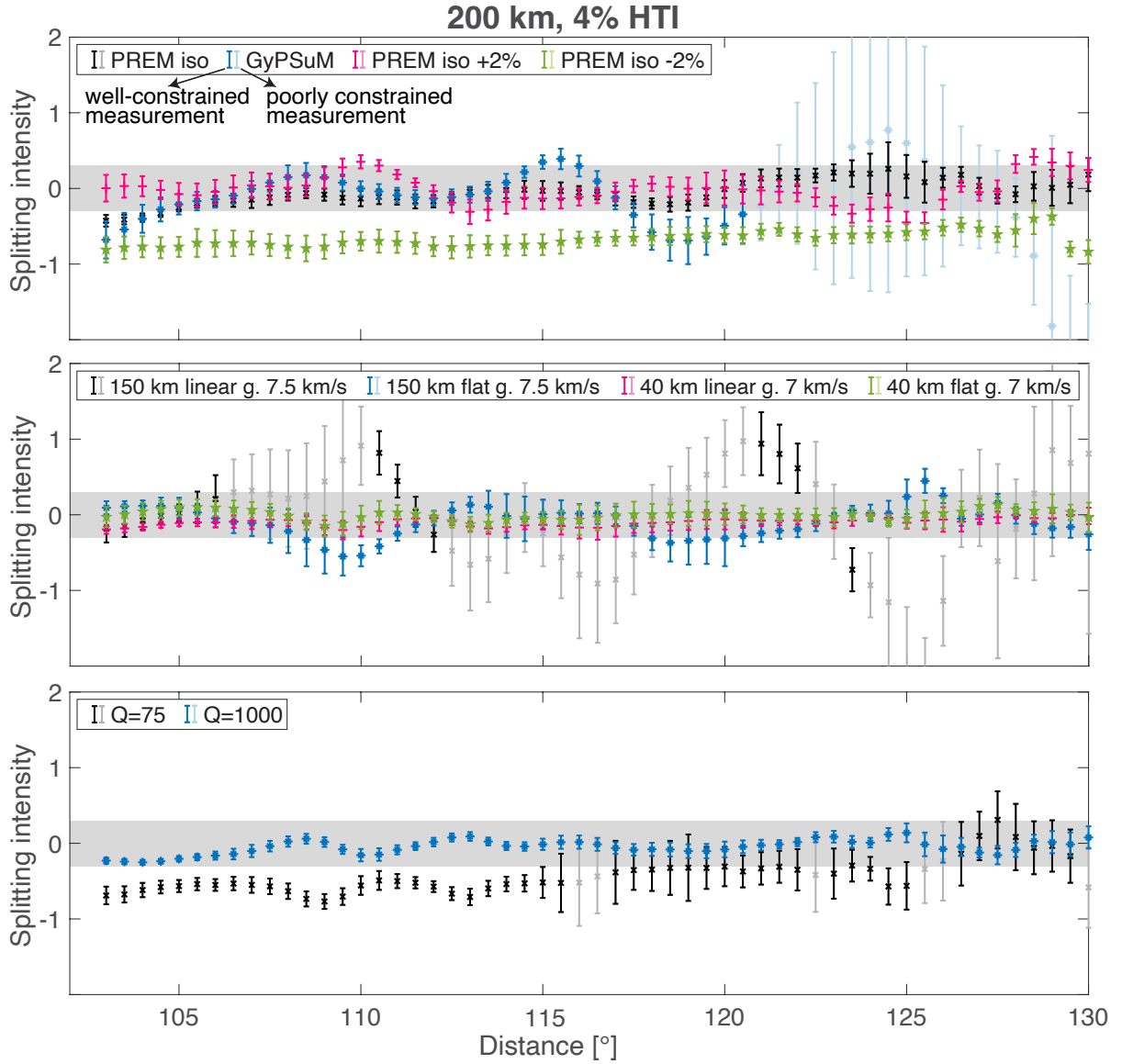


Figure S5: Results from similar simulations as those shown in Figure 8 of the main manuscript but for strong upper mantle anisotropy, plotted as  $SH_{\text{diff}}$  splitting intensities as a function of distance, calculated for a focal depth of 500 km.  $SI$  was measured using SplitRacer. 95% confidence intervals are indicated by error bars. Simulations for which the lowermost mantle velocity was modified are shown in the top panel. These include an input model for which the mantle in PREM has been replaced by the GyPSuM tomographic model (see legend). The middle panel shows results for different lowermost mantle velocity gradients, in particular, linear and flat gradients were tested (see legend). The bottom row presents results for two endmember  $Q$ -values. The shaded gray area indicates  $SI$ -values between  $-0.3$  and  $0.3$ , which would usually be defined as null.

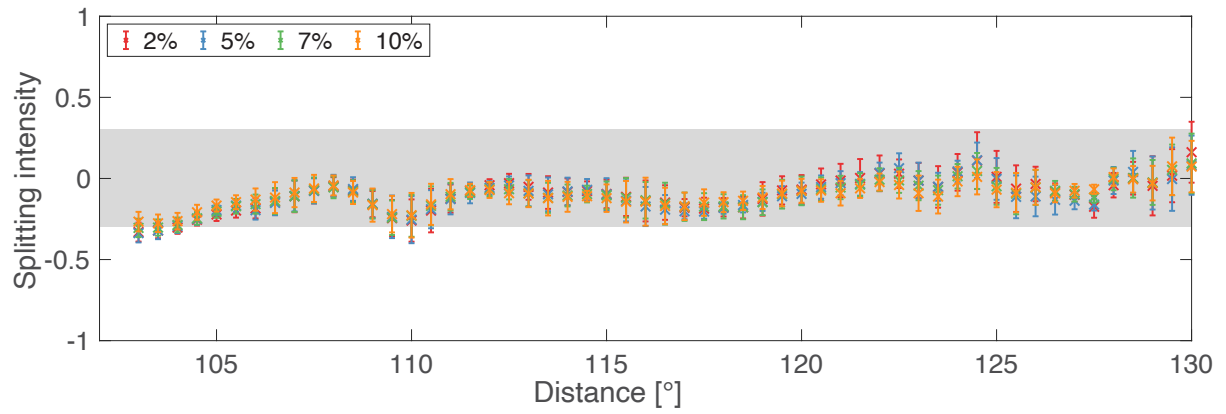


Figure S6: Similar to Figure 9 of the main manuscript for strong upper mantle anisotropy. Simulation results, expressed as measured splitting intensities, for initially SH-polarized  $S_{\text{diff}}$  waves for two different velocity reductions at the base of the mantle, calculated for a focal depth of 500 km. Plotting conventions are similar to Figure S9. Synthetics were computed for a 20 km thick low velocity at the base of the mantle. P wave velocity reductions are 1/3 of the S wave velocity reductions (see legend). 95% confidence intervals are shown by error bars. Almost all of the measurements are null. Results for other velocity reductions than those shown here are presented in Supplementary Figure S5.

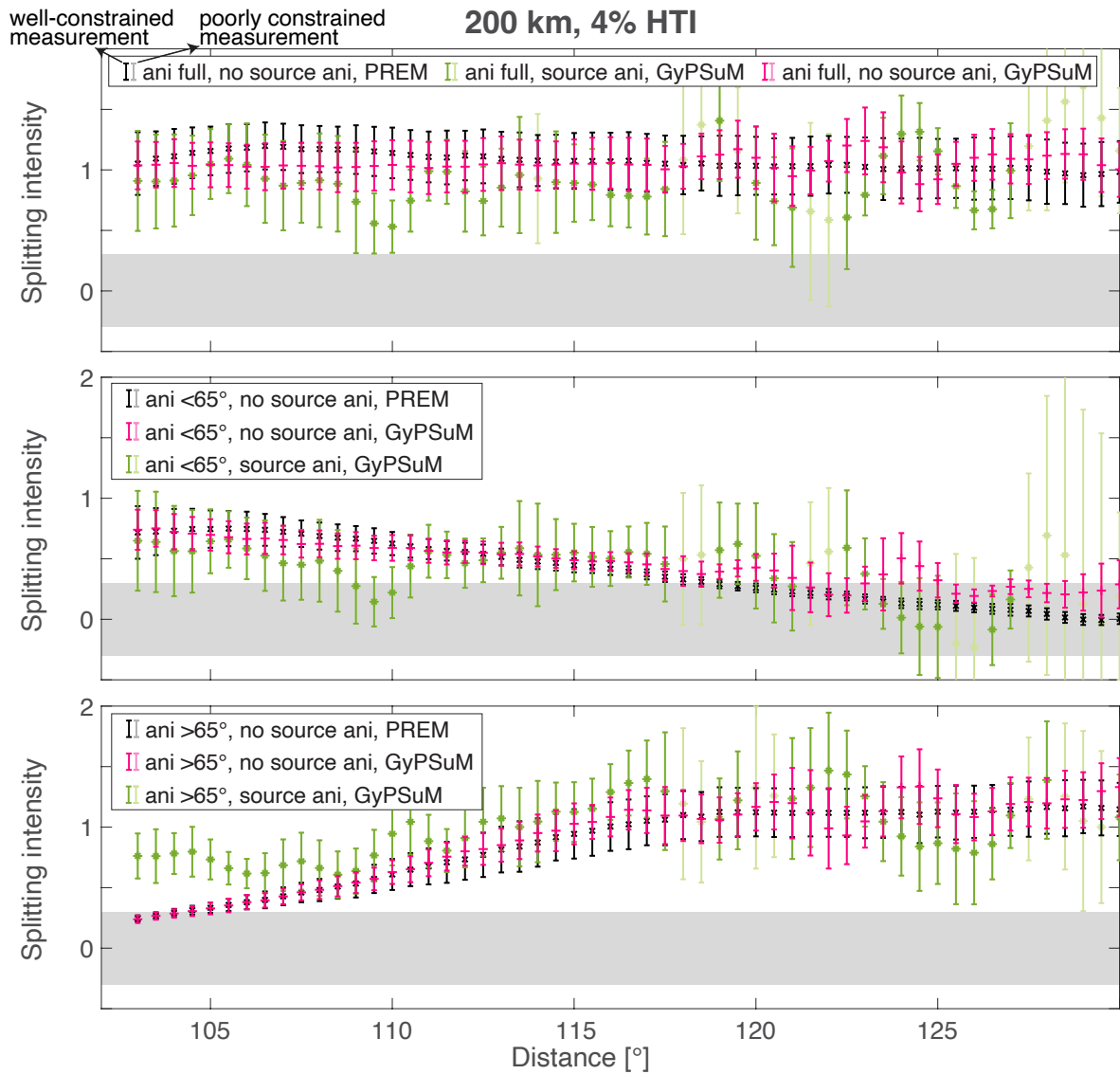


Figure S7: Similar to Figure 10 of the main manuscript for strong upper mantle anisotropy. Lowermost mantle anisotropy is incorporated for a full global layer of Ppv anisotropy, up to an epicentral distance of 65° (from the source) or from an epicentral distance of 65° (see legend). All simulations that use an isotropic PREM without GyPSuM include lowermost mantle anisotropy only (see legend). Simulations with GyPSuM tomography in the mantle (replacing PREM velocity structure) include source and receiver side anisotropy (see legend).

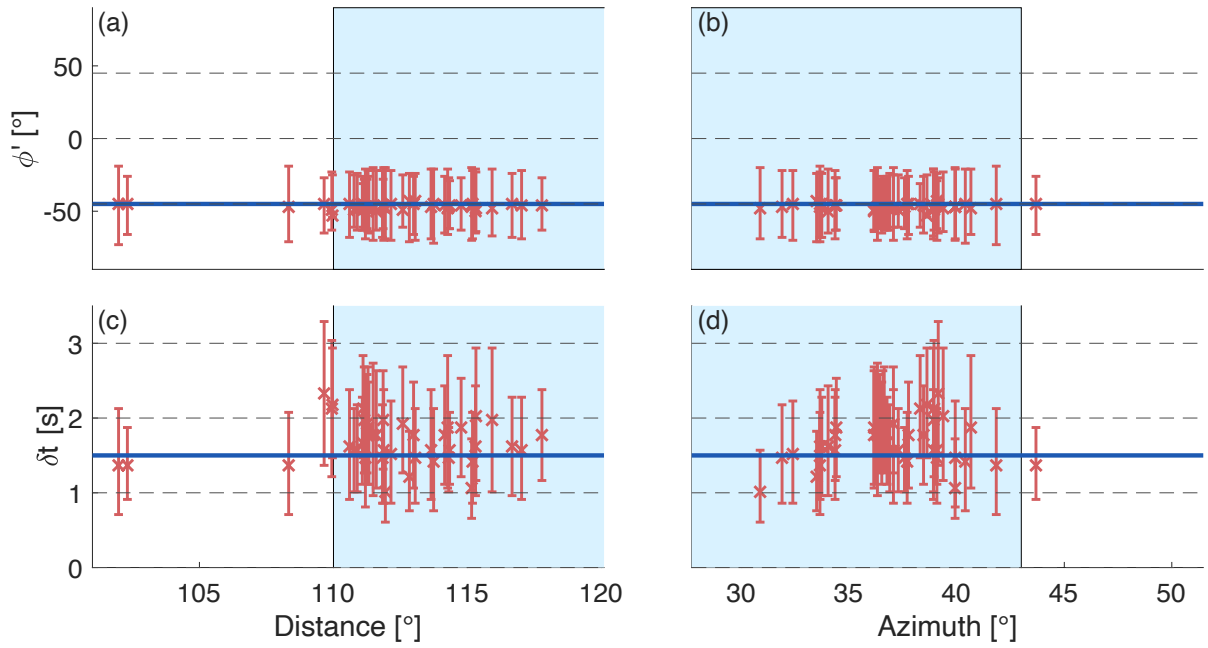


Figure S8: Well-constrained single station splitting parameters ( $\phi'$ ,  $\delta t$ ) for event 2009-10-04. (a-b)  $\phi'$  as a function of (a) distance and (b) azimuth. Red markers show best fitting fast polarization directions determined using SplitRacer; 95% confidence intervals are presented as error bars. The blue line shows the best fitting fast polarization direction measured from the stacked  $S_{\text{diff}}$  waveform from this event. Light blue shading indicates distances  $> 110^\circ$  and azimuths  $< 43^\circ$ , for which  $S_{\text{diff}}$  splitting was determined from stacks. (c-d) are analogous to (a-b) but for  $\delta t$ .

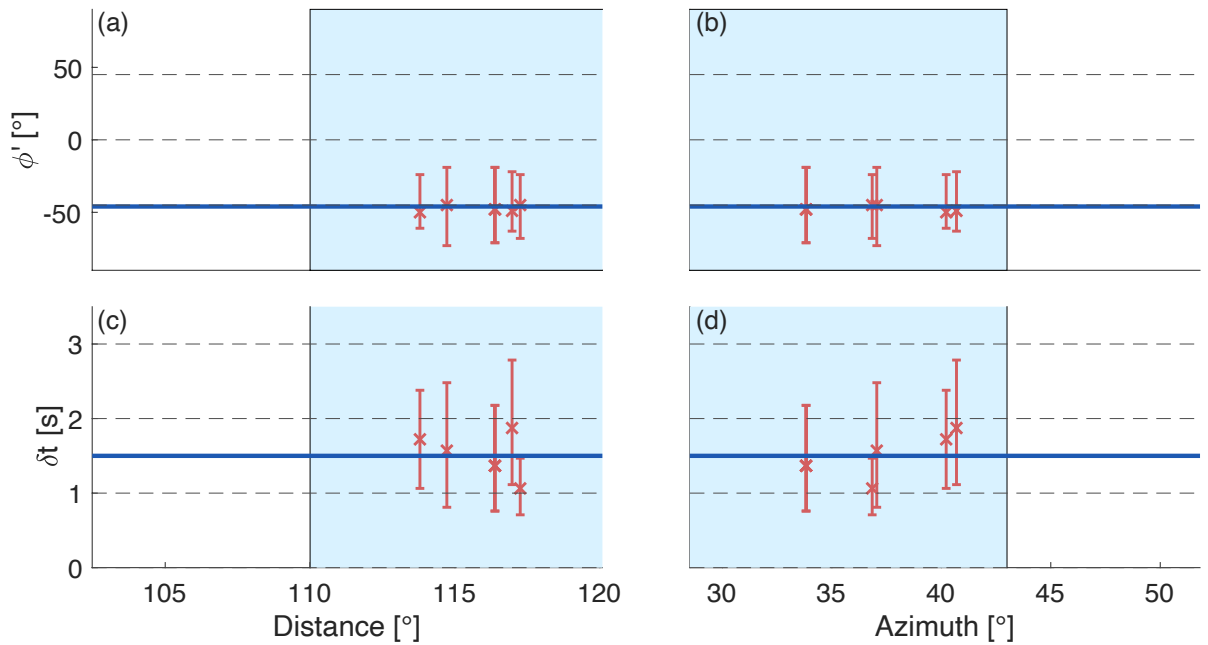


Figure S9: Like Figure S8 but for event 2009-10-07.

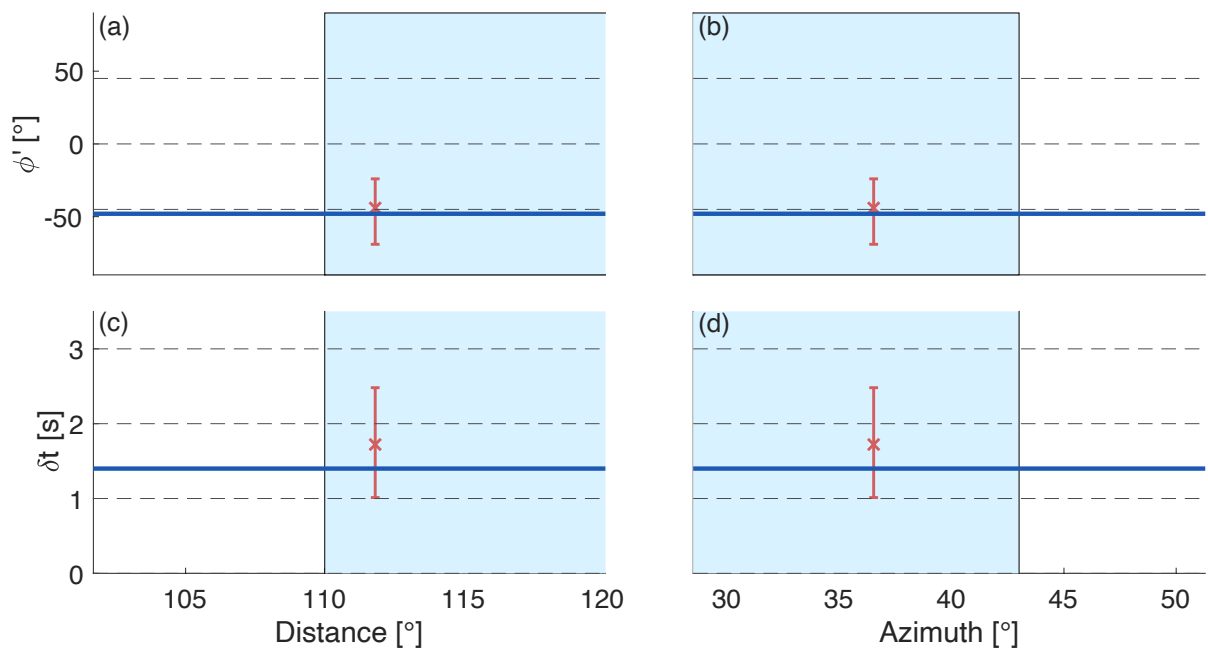


Figure S10: Like Figure S8 but for event 2010-10-24.

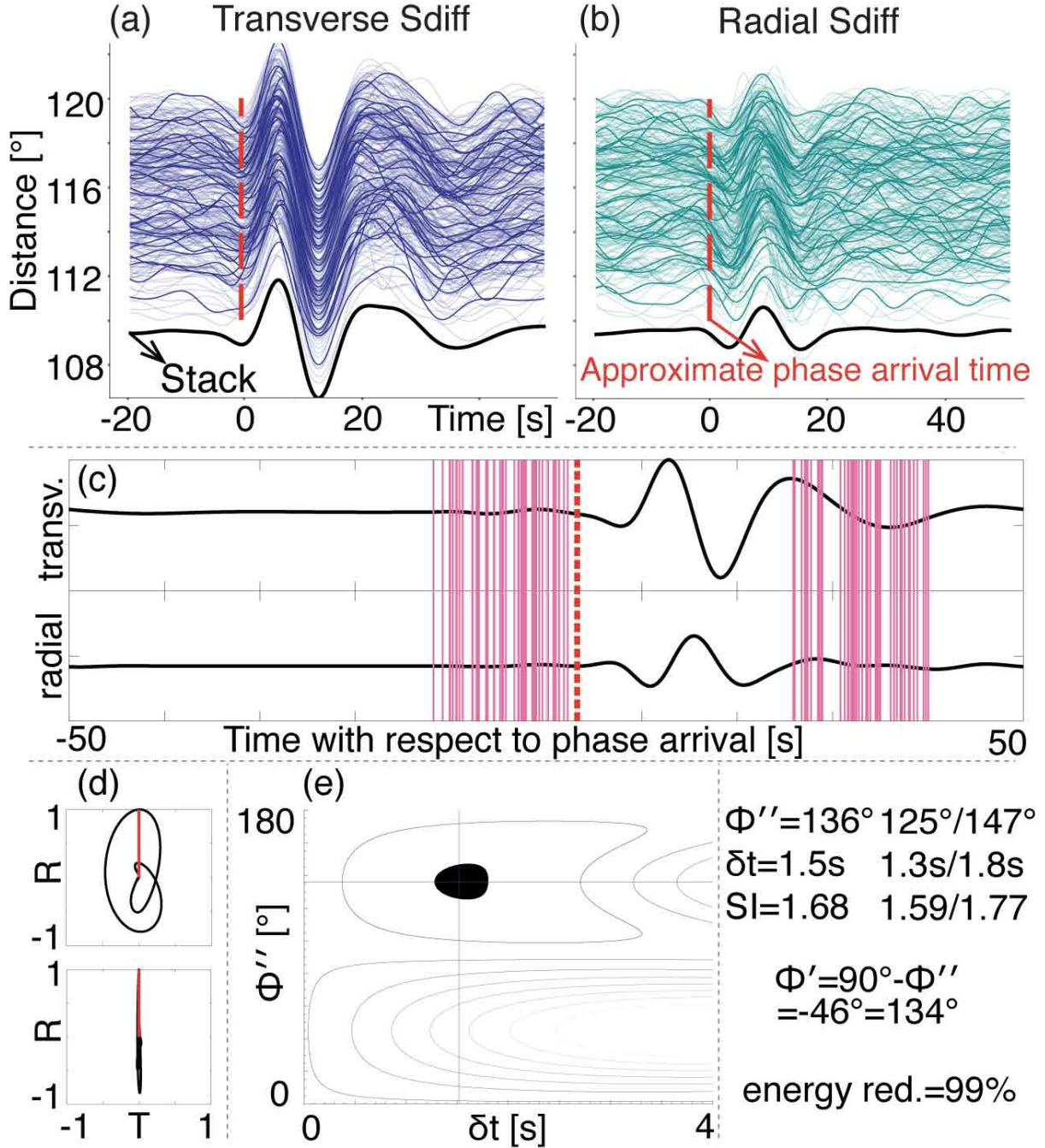


Figure S11:  $S_{\text{diff}}$  waveforms and splitting diagnostic plots from SplitRacer for event 2009-10-07. In the waveform plots, approximate  $S_{\text{diff}}$  arrival times are shown as a red dashed lines. (a) Transverse component waveforms recorded at a distance  $> 110^\circ$  and an azimuth  $< 43^\circ$  (see text). Waveforms were aligned and normalized with respect to the maximum transverse  $S_{\text{diff}}$  amplitudes. (b) Similar representation of the corresponding radial  $S_{\text{diff}}$  waveforms. Only every 10th trace is plotted without transparency to better visualize the individual waveforms. (c) Waveforms of the  $S_{\text{diff}}$  stack (radial, top trace; transverse, bottom trace) are shown as black solid lines and the start/end of the 50 randomly chosen measurement windows as pink lines. (d) The upper diagram shows the particle motion for the original stack, the lower diagrams for the waveforms that were corrected for splitting. The red lines in the diagrams indicate the backazimuthal direction. (e) The best fitting splitting parameters are shown in the  $\phi'' - \delta t$ -plane, with black color indicating the 95% confidence region. For an explanation of the splitting parameters  $\phi''$  and  $\phi'$  see Section 2.2 of the main manuscript.

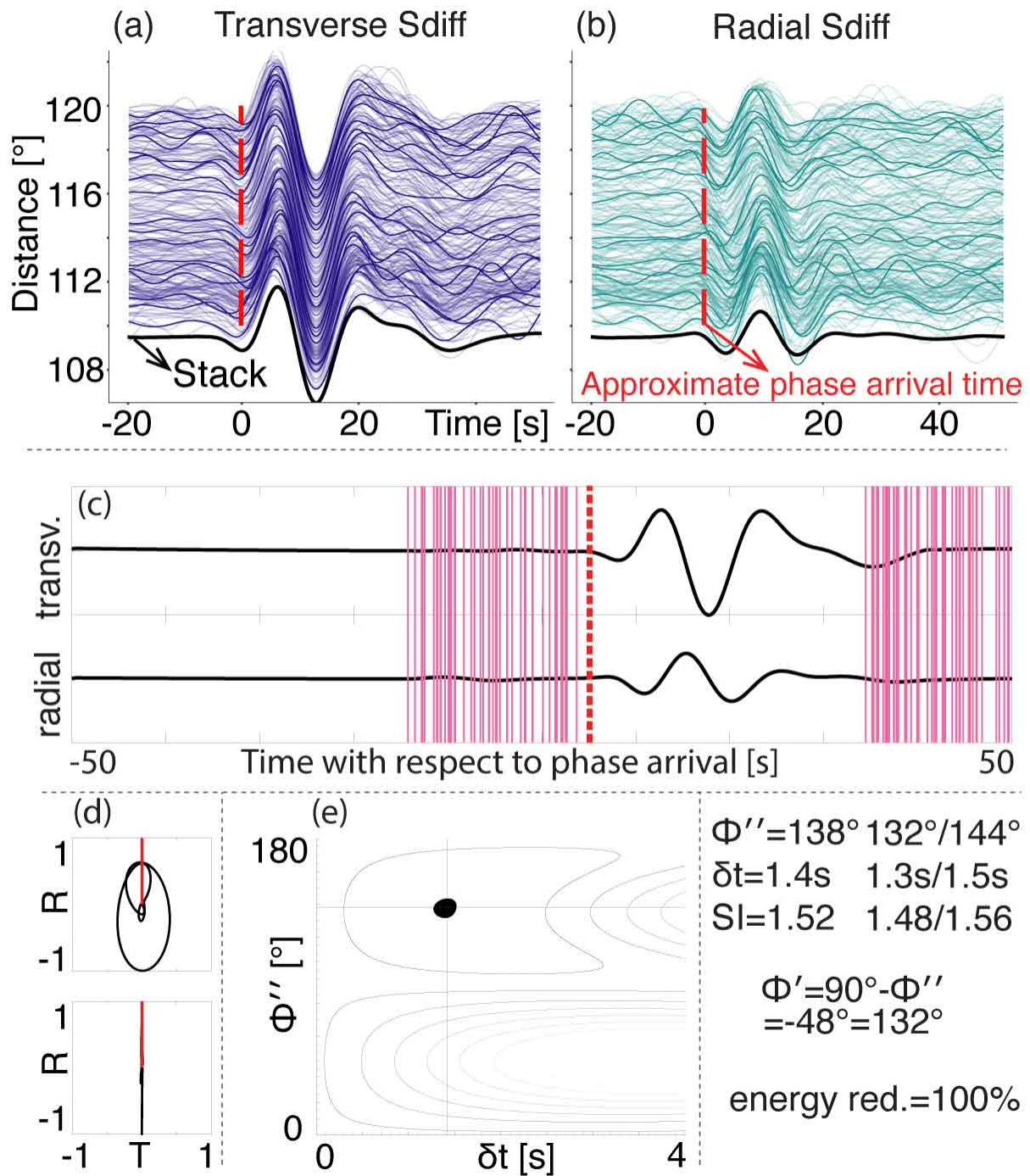


Figure S12: Same plotting conventions as in Figure S11 but here for event 2010-07-29.